LASER
& PHOTONICS
REVIEWS

Laser Photonics Rev. **9,** No. 5, 452–477 (2015) / **DOI** 10.1002/lpor.201500095

REVIEW ARTICLE

Abstract The progress on multi-wavelength quantum cascade laser arrays in the mid-infrared is reviewed, which are a powerful, robust and versatile source for next-generation spectroscopy and stand-off detection systems. Various approaches for the array elements are discussed, from conventional distributed-feedback lasers over master-oscillator power-amplifier devices to tapered oscillators, and the performances of the different array types are compared. The challenges associated with reliably achieving single-mode operation at deterministic wavelengths for each laser element in combination with a uniform distribution of high output power across the array are discussed. An overview of the range of applications benefiting from the quantum cascade laser approach is given. The distinct and crucial advantages of arrays over external cavity quantum cascade lasers as tunable single-mode sources in the mid-infrared are discussed. Spectroscopy and hyperspectral imaging demonstrations by quantum cascade laser arrays are reviewed.

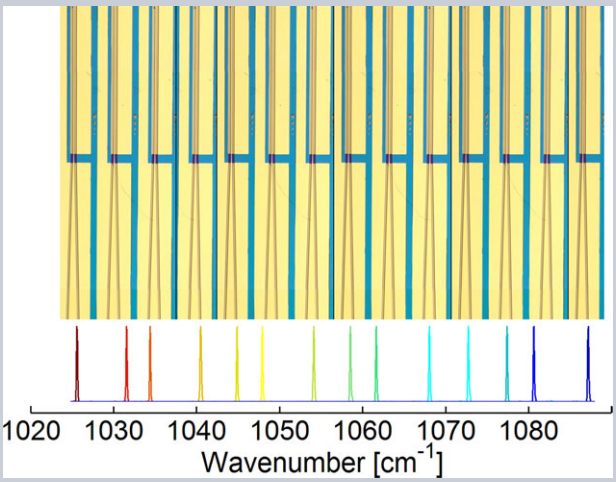

Multi-wavelength quantum cascade laser arrays

Patrick Rauter[1,2] and Federico Capasso[1,*]

1. Introduction

Since the first demonstration of a unipolar semiconductor laser based on cascaded intersubband transitions in an AlInAs/GaInAs heterostructure, quantum cascade lasers (QCLs) [1, 2] have continuously been attracting research interest from both applied and basic research communities. Steady progress has expanded the wavelength range accessible by QCLs, now extending from below 3 μm over the long-wavelength mid-infrared to the far-infrared and terahertz (THz) regime. In particular, the short-wavelength region poses significant challenges due to the large required confinement energies, which have been addressed by using material combinations with a high conduction-band offset such as InGaAs/AlAs(Sb) [3] or InAs/AlSb [4], or by implementing strain-compensated designs in the InGaAs/InAlAs-AlAs system [5]. In addition to the expanding range of operation wavelengths, the figures of merit achieved by QCLs have been continuously improved by refinement of the active material design and technological progress in growth and device processing, and have been further pushed by the implementation of novel concepts for bandstructure engineering and cavity photonics. The latter, e.g., include a novel phase-matching scheme for room-temperature THz-emission from QCLs based on difference-frequency generation [6], or the realization of plasmonic collimators achieving beams of high brightness [7]. The combined efforts from a multitude of groups have led to impressive figures of merit for QCLs in both the mid-infrared [8, 9] and THz regions [10, 11]. In the mid-infrared, room-temperature peak powers of up to 203 W have been demonstrated for large-area QCLs in multi-mode operation [12], while single-mode emission at peak powers up to 3.3 W and 34 W has been achieved by an angled-cavity broad-area distributed-feedback (DFB) QCL [13] and a photonic-crystal broad-area QCL [14], respectively, for pulsed operation in all three cases. For continuous-wave (cw) operation, mid-infrared DFB QCLs are reportedly capable of single-mode operation at 2.4 W of output power [15]. In the THz regime, broad-area THz QCLs have recently achieved peak output powers of more than 1 W [16], while for narrow ridges fabricated on wafer-bonded material with thick active regions peak powers of more than 500 mW have been reported [17]. The listed output power records achieved by state-of-the-art QCLs demonstrate impressively that these compact semiconductor laser sources have become the ideal source of coherent radiation for a large variety of applications, particularly when considering the tremendous degree of customization feasible due to the comprehensive design freedom for both the gain material and the device geometry. In this review article, we give an overview of recent progress in the development of multi-wavelength QCL arrays as next-generation sources of tunable, coherent, monochromatic radiation for spectroscopy and detection applications in the mid-infrared. In Section 2, we will illustrate the variety of applications, for which QCL-based systems can be employed by discussing a few selected publications on spectroscopy and

[1] Harvard University, School of Engineering and Applied Sciences, 29 Oxford St., Cambridge, MA 02138, USA
[2] Institute of Semiconductor and Solid State Physics, Johannes Kepler University Linz, Altenbergerstr. 69, 4040 Linz, Austria
*Corresponding author: e-mail: capasso@seas.harvard.edu

© 2015 by WILEY-VCH Verlag GmbH & Co. KGaA, Weinheim

sensing demonstrations. Section 3 briefly discusses the external cavity (EC) systems as a common, commercially available solution for QCL tuning, and the advantages and disadvantages of such platforms are highlighted. Moreover, Section 3 mentions a few alternative concepts for achieving tunable single-mode emission from QCLs, before introducing the concept of QCL arrays as a powerful alternative to EC QCLs. In the main part of this article, comprising Sections 4 to 9, the progress on multi-wavelength QCL arrays is reviewed, from DFB QCL arrays discussed in Section 4 over surface-emitting arrays in Section 5 to wavelength beam combining of the array output in Section 6. Section 7 finally reviews the very recent work on master-oscillator power-amplifier (MOPA) QCL arrays, which achieve multiwatt power levels for tunable single-mode emission at an excellent beam quality. In Section 8, recent studies on single-mode tapered QCLs as an alternative building block for moderate-power arrays are discussed. Spectroscopy and hyperspectral imaging demonstrations by QCL arrays are reviewed in Section 9 before concluding the review and offering perspectives on future developments in Section 10.

2. Quantum cascade lasers in spectroscopy and sensing applications

Recent years have seen the integration of QCLs as a source of mid-infrared or THz radiation in a large number of spectroscopy and sensing systems aimed at medical, environmental control, security and threat reduction or process monitoring applications [18]. In the following, examples of recent work in these fields will be mentioned to illustrate the spectrum of applications entered by QCLs. In medical instrumentation, breath analysis for diagnostic purposes is a promising field, where laser-based systems are developed as a low-cost, portable alternative to gas chromatography mass spectrometry [19]. In reference [20], the authors compare a QCL-based sensor for exhaled nitric oxide (NO), which is a biomarker for asthma, with electrochemical and chemiluminescence analyzers, concluding that QCL-based systems offer both portability and high sensitivities, thus outperforming the other two alternatives in one aspect or the other. In reference [21], a QCL is employed as a source coupled into a Ge waveguide integrated in a microfluidic chip for cocaine detection. The integration of the optical components required for sensing systems is taken one step further in reference [22], where a monolithic lab-on-a-chip for the mid-infrared has been demonstrated. Both the laser and detector device are fabricated from the same bifunctional active region material and couple to a surface plasmon polaritons waveguide. The latter allows a strong overlap of the guided mode with a liquid covering the chip, and detection capabilities for substances in solution in the parts per million (ppm) range have been predicted based on data from a proof-of-principle demonstration using ethanol in water. In reference [23], monitoring the concentration of nitric oxide, which is of high relevance for environmental control, with parts-per-billion sensitivities has been demonstrated for a QCL-based Faraday rotation spectroscopy system using an effective optical path length of only 44 cm.

Laser-based photoacoustic spectroscopy is another highly sensitive and robust gas detection technique, which in its most basic configuration requires high output powers in order to achieve detection levels required for environmental control systems. Using an EC QCL in a photoacoustic spectroscopy setup, nitrogen dioxide (NO_2), another routinely monitored pollutant and greenhouse gas, can be detected with a sensitivity of 0.5 parts per billion (ppb), as reported in reference [24]. Recently, a compact ($12 \times 5 \times 5$ inch) quartz-enhanced photoacoustic spectroscopy (QEPS) system based on a high-power cw DFB QCL for the detection of NO_2 and carbon monoxide (CO) has been demonstrated, achieving minimum detection limits of 23 and 1.5 ppb by volume (ppbv), respectively, with short sensor response times of less than 5 s [25]. QCL-based QEPS systems have very recently been used for measuring hydrogen peroxide (H_2O_2) [26], CO_2 [27] and nitrous acid (HONO) [28] concentrations with minimum detection limits down to 75 ppb, 300 ppt and 66 ppbv for integration times below 5 s, respectively. Both H_2O_2 and HONO are of environmental relevance and are commonly detected by disadvantageous wet chemistry methods.

Next to medical diagnostics and atmospheric pollutant control, the detection of gas traces in air can be employed in systems for security and threat reduction applications. Not only sensing of threats by volatile gases, but even the detection of solid explosives is feasible due to their finite vapor pressure at room temperature. The potential of QCL-based photoacoustic spectroscopy systems for the detection of TNT has been demonstrated in reference [29], with estimated minimum detection limits of TNT in air samples from the explosive surface down to 0.1 ppb, which is expected to enable TNT detection at sample temperatures down to 5 °C. The demonstrated system was based on a cw EC QCL and used a strong absorption line of TNT vapor around 7.3 μm wavelength, a spectral region inaccessible by CO_2 lasers, which are commonly used in photoacoustic spectroscopy systems. In addition to photoacoustic spectroscopy approaches to explosive detection, stand-off detection techniques based on infrared imaging of targets illuminated by tunable QCL sources are developed by several groups [30,31]. For this method, a HgCdTe focal plane array collects the QCL radiation diffusely backscattered by the target, while the laser wavelength is tuned in the spectral range containing characteristic absorption lines of the hazardous substances to detect. This results in so-called hyperspectral images, which are then analyzed by an algorithm extracting the scattering background from the carrier surface, before referencing the spectrum of the scattered radiation to a spectral databank. As demonstrated in reference [32], this detection scheme allows the identification and localization of explosives, where fingerprints of HMDT, PETN, and N-guanylurea-dinitramide on various real-life materials were tested. The clear detection of a 1-cm^2 spot of the latter at a stand-off distance of 20 m was reported, demonstrating the potential of QCL-based stand-off spectroscopy for field use in situations, where sampling

© 2015 by WILEY-VCH Verlag GmbH & Co. KGaA, Weinheim

of suspicious substances carries high risk. As also pointed out in reference [32], the low required average powers of the detection system of less than 3 mW and the spectral region of the employed QCL device ensure its eye safety. In addition to stand-off explosive detection, the authors of reference [32] report on the potential of external-cavity QCLs in another application, namely the in-line monitoring of water quality. Mid-infrared transmission spectroscopy of contaminants in liquids is particularly challenging due to the high absorption coefficient of water itself in this spectral region. As demonstrated in reference [32], the clear advantage of the use of QCLs over that of a Fourier-transform infrared spectrometer (FTIR) is the significantly increased optical path length in water feasible for the QCL-based system due to its high spectral power density, resulting in larger feasible dimensions (100 μm path length) of the flow cell and in a lower susceptibility to clogging.

QCL-based hyperspectral imaging is not only of interest for stand-off detection and security applications, but shows great potential as a basis of next-generation microscopy systems for digital pathology and cancer diagnosis. Very recent efforts by several groups have demonstrated that a QCL-based system for infrared imaging of tissue samples can reduce the scanning time of large tissue arrays by up to three orders of magnitude as compared to a common setup employing a FTIR. [33–35] All of these demonstrations were performed using a commercial EC QCL and conclude that the crucial advantage of the QCL-based microscopy system is the selective access to specific key wavelength regimes of interest for sample characterization in contrast to the comprehensive collection of spectral information intrinsic to the FTIR approach. The drastic increase in sample scan rate achieved by QCL microscopes in the mid-infrared has the potential to enable a wide-spread adoption of infrared spectral diagnosis in the clinical setting and to revolutionize digital spectral pathology.

All of the listed publications demonstrate the potential of QCLs for spectroscopic applications, where these compact and versatile semiconductor lasers hold distinct advantages in crucial and customizable aspects over alternative sources like incoherent emitters, diode lasers or gas lasers.

3. Tunable quantum cascade laser sources

3.1. Broadband QCL material

Many of the applications discussed in the previous section require the tunability of the employed mid-infrared source over a certain wavelength range. Even for highly specialized detection schemes relying on a specific absorption line of only one particular molecule in gas form, data acquisition at multiple wavelengths increases the reliability of detection by enabling distinction between gases with similar absorption fingerprints. The latter becomes absolutely crucial for simultaneous probing of multiple substances with a low error rate. The basis of tunable laser systems is broadband gain, and extensive research efforts by various groups have been expanding the gain bandwidth available in QCL active regions, achieved mainly by engineering the number of optical transitions reaching population inversion. QCL material based on a bound-to-continuum design [36], with a number of different final states for lasing, can feature broadband gain of a full width at half-maximum (FWHM) between 200 and 300 cm^{-1}, where a refined design for high-performance lasers has been presented in reference [37]. A different approach for reaching ultra-broad gain is based on growing tens of different cascade sections while maintaining conditions for efficient injection between the sections, with each section lasing at a slightly different wavelength [38]. The heterogeneous cascade approach applied in reference [39] reduces the number of different sections to two, thus simplifying growth and still achieving a gain FWHM of 290 cm^{-1} in a material suited for external cavity systems. In reference [40], the authors introduce a second upper state for lasing into a homogeneous bound-to-bound cascade design, achieving a gain FWHM of about 300 cm^{-1}. The authors in reference [41] expand the gain bandwidth available in a homogeneous cascade structure by increasing the number of upper states for lasing in a continuum-to-continuum design, resulting in a gain FWHM of 430 cm^{-1}.

Thus, QCLs based on broadband gain material can cover a spectral range in the fingerprint region of a target substance large enough for a thorough referencing to chemical databases and the elimination of detection errors. However, the spectroscopy and detection schemes discussed above require single-mode operation of the employed QCL source, which can be reliably achieved by implementing an index grating for wavelength selection in DFB configuration [42]. Even though DFB QCLs are capable of pulsed or cw operation with high beam quality and excellent figures of merit, their tunability is very limited. As the first-order grating for wavelength selection of a DFB laser is defined during fabrication and thus has a fixed periodicity, tuning can only be achieved by a temperature-induced change in the refractive index, limiting the tunability to a few cm^{-1}.

3.2. External cavity QCLs

At present, the need for tunable single-mode QCLs for spectroscopic applications is therefore commonly fulfilled by EC QCLs [43]. Since the first demonstration of broadly tunable EC QCL operation [44], EC QCLs have been realized for various wavelength regimes and based on a number of different active region designs. Tunability over more than 430 cm^{-1} and 550 cm^{-1} has been demonstrated in the 7–11 μm [45] and 3–4 μm [46] windows, respectively. EC QCLs are capable of several tens of mW cw output power, have been employed in countless spectroscopy and sensing demonstrations, and are commercially available. However, due to their setup, size and mechanical tuning, they face a number of serious limitations concerning field applications, as discussed in the following.

EC QCL systems comprise a QCL device, fabricated from material featuring broadband gain, a lens for

© 2015 by WILEY-VCH Verlag GmbH & Co. KGaA, Weinheim

collimating the QCL output into a parallel beam and a grating providing wavelength-selective feedback. An antireflection (AR) coating is applied to one of the QCL facets to enable the formation of an external cavity without significant coupled-cavity effects. The configuration commonly used in EC QCL setups is the so-called Littrow configuration, where the parallel QCL output beam hits a movable grating. By adjusting the angle of the grating with respect to the output beam direction, the first-order diffracted beam of the desired wavelength is coupled back into the AR-coated QCL facet. Due to this feedback, an external cavity is formed, and lasing at the wavelength of choice can be achieved. The zero-order beam of the grating is used as an output of the system. By rotating the grating, the wavelength condition for providing feedback is changed, and the output wavelength of the EC QCL can be tuned, ideally over the entire gain region. In more advanced system geometries [43, 47], a movable mirror is added to the setup, and rotating and translating both the grating and the mirror prevents walk-off of the output beam during tuning. These rotation and translation operations can be reduced to rotating one platform, on which both the grating and mirror are mounted, requiring meticulous alignment of all components. In an alternative variation of the Littrow configuration [30], the external grating couples to the *back* facet of the QCL, which intrinsically avoids the beam-walk-off issue. However, this configuration does not allow the application of a high-reflectivity coating to the QCL facet not facing the grating, and the intensity in the grating diffraction order usually employed as the system output is lost. Furthermore, the mode-hop free tuning of an EC QCL over a wide wavelength range reported in reference [47] required precise control of the cavity length in order to fulfill the round-trip conditions for the wavelength selected by the grating angle. This manipulation of the EC length is achieved by mounting the rotating grating+mirror-platform on a piezoactuated translation stage and implementing cavity mode tracking. Thus, even though EC QCLs are capable of impressive tunability and figures of merit, their means of mechanical tuning poses a serious challenge for field applications. The systems have to be carefully aligned, and the mechanical components are sensitive to vibrations or harsh movements, making them too delicate for vehicle-mounted or portable systems. The considerable challenge in achieving mode-hop free tuning even in an ideal and vibration-free environment further limits the use of these systems. For many field applications in sensing and spectroscopy, ruggedness, compact size and low weight take priority over a large tuning range or high average power. Ideally, systems for field use would be based on a compact monolithic source, which can be electrically tuned, is free of moving parts and requires a number of external optical components as low as possible. The latter calls for a high beam quality of the direct output from the source chip, and would benefit from integration of the laser with optical components for beam collimation or beam combining. In this article, we review the progress on realizing such monolithic, electrically tunable, single-mode QCL sources in the form of multi-wavelength laser arrays. Before presenting the work of our group on DFB QCL arrays, high-power master-oscillator power-amplifier arrays and tapered oscillator/distributed-Bragg-reflector QCLs, a brief discussion of two single-element alternatives to EC QCLs for spectroscopy applications is given.

3.3. Alternative single-device solutions for wavelength tuning

One concept that aims at providing electrical wavelength tunability of single-mode emission from a monolithic device is that of sampled grating reflectors integrated with a QCL gain region [48]. The two grating reflectors, which were defined by electron beam lithography and subsequent etching and cladding regrowth, have slightly different periods, causing an overlap of their reflectivity spectra at only one wavelength in the gain region. For modes of this overlap wavelength, the gratings form a cavity, and lasing is possible. Tuning of the coincidence wavelength is possible in a Vernier-like fashion by changing the temperature of one of the reflectors via current-induced heating. Recently, discrete wavelength tuning over 236 cm^{-1} was achieved for such a device, with output powers of hundreds of milliwatts at most wavelengths and a side-mode suppression ratio (SMSR) of at least 20 dB [49]. However, the demonstrated three-section devices are rather complex in operation, commonly exhibiting deviations of the observed tuning behavior from the theoretically predicted characteristics due to gain competition and spatial hole burning effects. Very recently, an improvement in tuning stability of sampled grating QCLs has been demonstrated by thoroughly choosing the loss margin required for the suppression of unwanted modes in a device with AR-coated facets. [50]

There are alternative spectroscopy concepts, which circumvent the need for a broad tunability of single-mode emission by relying on simultaneous illumination of the test specimen with a multi-wavelength laser spectrum and a subsequent interference process. This spectroscopy approach is referred to as multiheterodyne spectroscopy [51, 52] or time-domain spectroscopy [53], and is based on the interference of two beams (signal and local oscillator beams) on a fast detector, where each beam features a mode-locked series of equally spaced, narrow intensity peaks (a so-called frequency comb). The two frequency combs have slightly different frequency spacings, resulting in a heterodyne beat and generating a beat note of the detector signal in the radiofrequency (RF) domain. A Fourier transform of the time-domain detector signal gives a RF spectrum, which reproduces the optical spectrum of the signal beam. In multiheterodyne spectroscopy, the optical spectrum is thus "downsampled" into the RF regime, and absorption spectroscopy of a target substance can be performed by passing the signal beam through the specimen. Frequency-comb spectroscopy delivers impressive results in the near-infrared, with short acquisition times, high signal-to-noise ratios and excellent resolution. Very recently, there has been significant progress towards achieving a mode-locked frequency comb and emission of ultrashort pulses from a QCL.

© 2015 by WILEY-VCH Verlag GmbH & Co. KGaA, Weinheim

In references [54, 55], mid-infrared frequency combs generated by a free-running QCL have been demonstrated, where the phase-locking between the individual modes is achieved by four-wave mixing in the active material. Very recently, broadband frequency comb formation in a THz QCL has been demonstrated, supported by a chirped corrugation etched into the cavity facet for dispersion compensation [56]. The authors in reference [57] propose a method based on an external ring cavity for achieving robust active mode locking in a mid-infrared QCL. In reference [58] such an external ring-cavity QCL has been demonstrated as a first step towards a mode-locked mid-infrared QCL independent of cryogenic cooling, and suppression of spatial hole burning and single-mode emission has been observed. In reference [59], QCL-based multiheterodyne spectroscopy has been demonstrated by employing two Fabry–Perot QCLs with slightly different free spectral ranges instead of a true frequency comb, achieving a spectral resolution of 15 MHz during a spectroscopy demonstration on NH_3 and N_2O. However, the spectral range available for spectroscopy in this configuration was very limited, and is for such a system intrinsically restricted to the region of overlap between two given Fabry–Perot spectra of different cavities. Very recently, the first dual-comb spectroscopy demonstration based on quantum cascade lasers has been reported, with an achieved bandwidth of 16 cm^{-1} and a high spectral resolution of 0.0027 cm^{-1} [60]. While the presented setup suffers from gaps in the spectral coverage due to peak-to-peak intensity variations in the frequency combs and from a relatively narrow bandwidth, the reported results clearly indicate the large potential of multiheterodyne spectroscopy employing a QCL frequency comb, which could challenge EC QCLs as a convenient platform for mid-infrared detection.

3.4. Quantum cascade laser arrays

In this article, we will review the progress on an alternative approach to QCL-based sources for mid-infrared spectroscopy: We will discuss the advances in the field of multi-wavelength QCL arrays. The basic concept is straightforward: For realizing a monolithic single-mode source tunable over a broad wavelength regime, a number of different single-mode QCLs is fabricated from a broadband material on a single chip, all lasing at a different wavelength spanning the desired region, and ideally featuring a wavelength spacing smaller than the feasible range of temperature tuning. Challenges arise from the high levels of control over mode selection crucial for the realization of such a chip, as the performance requirements dictated by the specific target application have to be met by all of its devices.

In addition to the multi-wavelength array approach reviewed here, the concept of integrating a number of interplaying QCLs on a chip to form an array has been implemented to pursue power-upscaling, and a number of groups have demonstrated phase-locked arrays of QCLs in the mid-infrared [61–63] and THz [64] regions. The goal of these phased QCL arrays is to achieve coherence between the array elements' emission, resulting in a narrow and stable far-field of high brightness, while maintaining the efficient heat management of narrow small-area devices. The challenges for these arrays are thus different from those faced for multi-wavelength arrays, where coupling between individual devices is of no interest and of minor concern, as sequential firing of individual devices of different design is targeted. However, the tree-shaped combining of QCL ridges demonstrated in reference [62] is of potential interest for multi-wavelength arrays, as future concepts can include monolithic beam combining of the elements of a multi-wavelength array, paving the road towards fully integrated, tunable single-mode sources of high beam quality.

4. Distributed feedback quantum cascade laser arrays

4.1. Wavelength selection

The realization of a multi-wavelength array of single-mode QCLs requires reliable means of selecting a different wavelength for each individual element. For QCLs, the most successful and commonly applied concept for longitudinal mode selection is that of distributed feedback [42, 65]. In the following, the concept is briefly described, as a basis for more indepth discussions later on. The DFB and MOPA QCL arrays discussed in the following are based on predominantly index-coupled gratings, as opposed to loss coupling. For achieving single-mode lasing at a selected wavelength within the gain region of the QCL material, an index grating with a periodicity p equal to half of the desired wavelength in the medium is fabricated into the top of a QCL ridge, spatially overlapping with the region of mode confinement in order to provide feedback. This is usually achieved by removing the top cladding of the QCL material, defining a grating by electron beam or interference lithography, and etching into the exposed material, which is of higher refractive index than the cladding. The cladding is then commonly regrown, although DFB QCLs without regrowth of a cladding are realized as well. Due to the resulting periodic variation in the refractive index, a photonic bandgap opens up around the Bragg frequency $\omega_0 = \pi c/(p \cdot n_{\mathrm{eff}})$, where c is the speed of light and n_{eff} the effective refractive index of the waveguide. The operation of a DFB grating formed by the corrugated surface in the QCL material is influenced by a number of parameters like its depth, its duty cycle, its overlap with the waveguide mode and the index contrast between the etched material and the regrown material. The combined influence by these parameters defined during fabrication manifests itself in one macroscopic figure, the difference in (complex) effective refractive index between the low- and the high-frequency DFB modes, $\Delta(n_{\mathrm{eff}} + \mathrm{i}\, k)$. The closely related figure commonly used to quantify the coupling between the left- and right-travelling waves in coupled mode theory is the coupling coefficient κ, defined by $\kappa = \pi\, \Delta(n_{\mathrm{eff}} + \mathrm{i}\, k)/\lambda_0$, where λ_0 is the Bragg

© 2015 by WILEY-VCH Verlag GmbH & Co. KGaA, Weinheim

wavelength of the grating. Note that for a sinusoidal spatial modulation of the refractive index in a dominantly index-coupled grating, κ relates to the modulation amplitude n_1 as $\kappa = \pi n_1/\lambda_0$ [66]. For gratings with more complicated grating profiles, the coupling coefficient can be determined following a decomposition of the squared spatial index variation into a Fourier series. As the width of the photonic bandgap $\Delta\nu$ (in cm^{-1}) is given by $\Delta\nu = \Delta n_{\mathrm{eff}}/(n_{\mathrm{eff}}\ \lambda_0)$, the real part of the coupling coefficient and the width of the photonic bandgap are related as $\mathrm{Re}(\kappa) = \pi \cdot n_{\mathrm{eff}} \cdot \Delta\nu$. Now, the coupling coefficient of a DFB grating in combination with its interaction length determines the envelope of the intensity profile of the DFB modes along the cavity. The dimensionless parameter κL, often referred to as the coupling strength, is commonly used to distinguish between different coupling regimes, with different associated intensity distributions inside a laser cavity. The modes at the two edges of the photonic bandgap, exactly at the points of vanishing group velocity $v_g = \delta\omega/\delta k$, are equivalent to standing electromagnetic waves in the waveguide. Both the low- and the high-frequency mode at the bandgap edges can be selected for lasing. However, even for a predominantly index-coupled grating the two DFB modes are subject to losses of different magnitude, favoring lasing of one mode over the other. In a DFB QCL, the low-frequency mode is more localized in the high-index material of the grating (the GaInAs grating host layer), while the high-frequency mode has higher field components in the low-index material (the InP cladding layer). Depending on the losses present in the individual materials, one of the two bandgap modes is favored for lasing. Usually, losses due to free-carrier absorption are higher in the GaInAs grating host layer than in the InP cladding, resulting in predominant lasing on the high-frequency mode for most DFB QCLs. However, the influence of device facets can result in more complex mode-selection mechanisms in DFB QCLs, as discussed in Section 4.3.

4.2. Distributed feedback quantum cascade laser arrays: Performance

The first demonstration of a multi-wavelength QCL array was reported by our group in 2007, when an array of 32 DFB QCLs on a chip was realized [67]. An electron micrograph and photograph of the array, which had a footprint size of $4 \times 5\ \mathrm{mm}^2$, are shown in the insets of Figs. 1a and b, respectively. The array was based on a bound-to-continuum material design with broadband gain around 9 μm first reported in reference [68], which showed a FWHM of the electroluminescence spectrum of about 300 cm^{-1}. In order to achieve lasing at a series of wavelengths within the broad gain region of the material, 32 DFB gratings of different periods between 1.365 and 1.484 μm were defined by optical lithography and subsequent etching. The fabricated QCL elements featured a ridge width of 15 μm, and were 3.5 mm long with a spacing of 75 μm between the individual lasers. All of the array elements were capable of single-mode operation, and the chip allowed switching between 32 different wavelengths between 8.73 and 9.43 μm, spaced by about 2.75 cm^{-1}. For all of the 32 wavelengths, a side-mode suppression of at least 20 dB was achieved. Figure 1a shows normalized emission spectra for each of the 32 QCL array elements in reference [67]. All devices lase at equidistant frequencies, and thus consistently operate on one side of the photonic bandgap, which was identified as the high-frequency side. The deterministic lasing on the high-frequency DFB mode was achieved by realizing overcoupled DFB gratings with $\kappa L \sim 11$ for the 3.5-mm long devices. A thorough study on the dependence of the mode selection on the coupling strength was presented in a follow-up publication [69], and is discussed in Section 4.3.

Discrete wavelength tuning of the single-mode output of this monolithic QCL source by switching between the individual array elements was carried out via a custom-designed microcontroller, which was employed for driving the array chip in pulsed operation. A photograph of the microcontroller setup is shown in the inset of Fig. 1c. In addition to sequential firing of individual elements, each QCL element could be continuously temperature tuned over several cm^{-1}. By employing a combination between switching and temperature tuning, the demonstrated array was capable of single-mode output continuously tunable over the whole spectral range between 8.73 and 9.43 μm (spanning 85 cm^{-1}). The operation of the QCL DFB array demonstrated in reference [67] was limited by strongly varying slope efficiencies between the individual elements between 20 and 200 mW/A and a consequential inhomogeneity in achievable output power over the spectral range accessible by the chip. This variation in output power between the individual QCLs is a significant drawback for the array performance, where the cause of this behavior was attributed to the device facet influence on mode selection in reference [67] (see next section).

In 2009, a DFB QCL array of greatly extended tuning range was demonstrated [70]. The chip was based on a heterogeneous cascade including two different bound-to-continuum designs [39] with a gain FWHM of 350 cm^{-1}. This array achieved an impressive tunability over 220 cm^{-1}, with the possibility to electronically switch between single-mode operation (>20 dB SMSR) at 25 different wavelengths ranging from 8 to 9.8 μm. The individual array elements once again operated in the overcoupled regime, with $\kappa L \sim 9$, achieving lasing on the high-frequency DFB mode for all of the devices and an equidistant wavenumber spacing of 9.5 cm^{-1}, as seen from the plot of the respective spectra in Fig. 1b. However, like the array presented in reference [67], this broadband array showed a large variation in slope efficiency between the elements, with accessible peak powers in pulsed operation spreading between 130 mW and 1.2 W.

In addition to the developments on arrays of QCLs with buried refractive index gratings in our group, efforts on the realization of arrays based on metal-plated surface gratings have been recently reported in conference contributions by Carras et al. [71] The DFB gratings of the laser elements in

© 2015 by WILEY-VCH Verlag GmbH & Co. KGaA, Weinheim

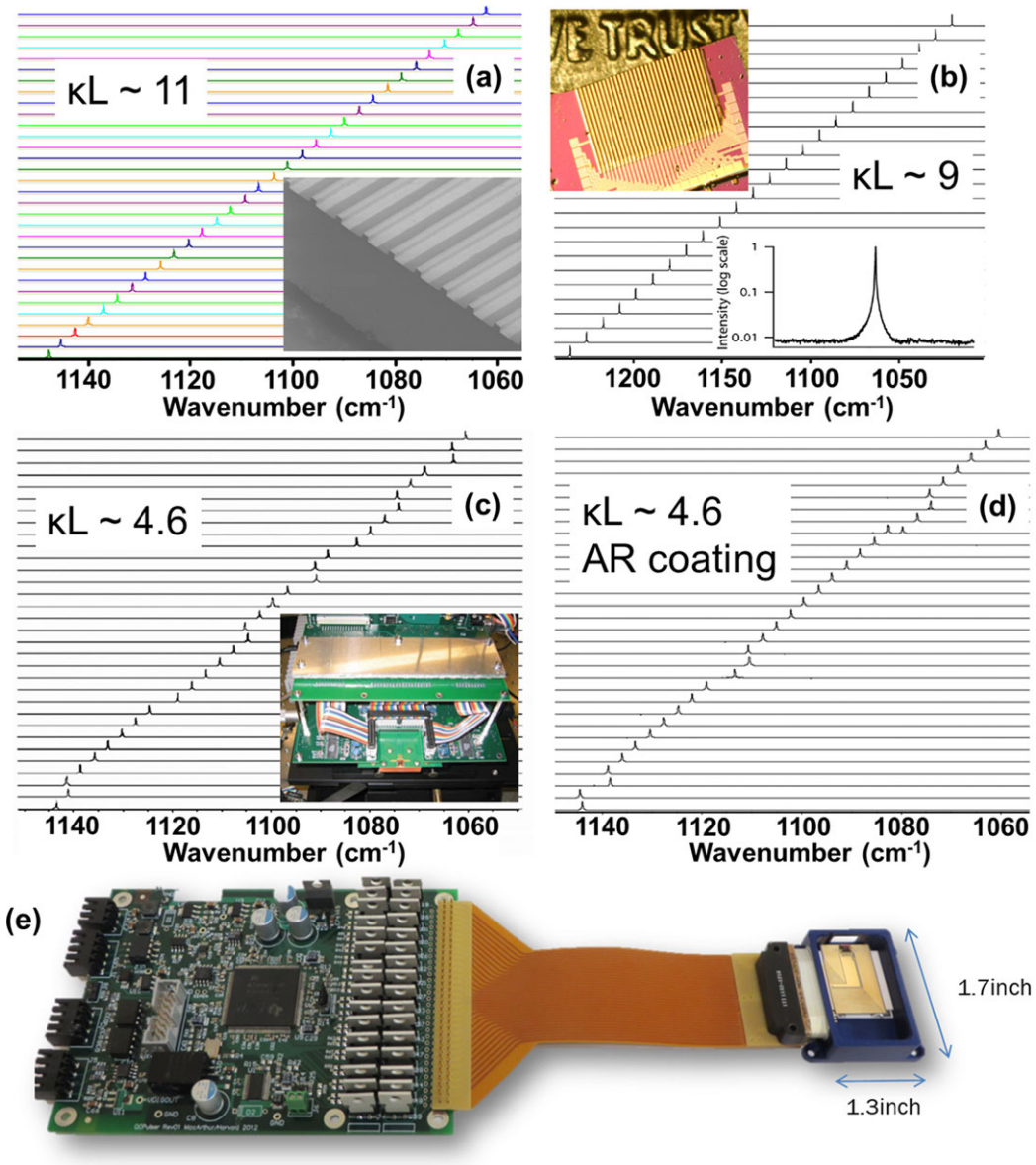

Figure 1 Distributed feedback quantum cascade laser arrays. (a) Normalized emission spectra for each element of the first demonstrated DFB QCL array. The inset shows an electron micrograph of several laser ridges of the array. (b) Extended spectral coverage achieved in a broadband DFB QCL array. The insets show a top-view image of a DFB QCL array and a logarithmic plot of a representative single-mode spectrum. The equidistant wavenumber spacing for the arrays in (a) and (b) was achieved by deterministic lasing at the high-frequency DFB mode for all array elements due to an overcoupling grating with $\kappa L \sim 11$ and $\kappa L \sim 9$, respectively. (c) For arrays with moderately coupled DFB gratings ($\kappa L \sim 4.6$), the influence of the device facets on mode selection results in lasing on the low-frequency DFB mode for several elements. The inset shows the custom-made microcontroller employed for switching between the individual array elements to achieve purely electronic wavelength tuning of the single-mode array emission. (d) Applying an AR coating to one device facet of an array with moderate DFB coupling reduces the device-facet influence and the number of elements lasing on the low-frequency DFB mode. (e) Photograph of a compact commercial DFB QCL array prototype system. Source: EOS Photonics. (a) Reproduced with permission [80]. Copyright 2009, SPIE. (b) Reproduced with permission [70]. Copyright 2009, IEEE. (c,d) Reproduced with permission [69]. Copyright 2009, IEEE. (e) Reproduced with permission. Copyright 2014, EOS Photonics.

this approach feature a complex coupling coefficient and do not require an additional cladding growth step after grating definition. While cw operation with 20 mW of single-mode output power was reported for individual QCLs based on surface gratings by the same group at the III-V Lab [72], no performance characterization of an array has been published up to now.

Very recently, DFB QCL arrays for spectroscopic applications have become commercially available, where an image of a prototype system is shown in Fig. 1e.

© 2015 by WILEY-VCH Verlag GmbH & Co. KGaA, Weinheim

To summarize this section, DFB QCL arrays are compact and rugged sources of single-mode emission, tunable over a wide wavelength range limited only by the gain profile of the active region. These continuously tunable sources of coherent mid-infrared radiation are independent of moving components, and tuning is achieved in a purely electronic way by switching between the individual array elements and by current control of the device temperature. This nonmechanical tuning mechanism gives QCL arrays a tremendous advantage over EC systems, and qualifies them for field applications as well as applications requiring maintenance-free operation in challenging conditions.

4.3. Distributed feedback quantum cascade laser arrays: Device facet influence

As mentioned above, the selection of the lasing wavelength in the demonstrated DFB QCL arrays relies on a predominantly index-coupled grating, where the grating-induced spatial variation of the waveguide losses does not contribute significantly to the coupling coefficient. The discussed DFB QCL arrays were based on conventional designs for refractive index gratings without particular efforts on increasing the loss difference between the two DFB modes. For the QCL arrays reported in reference [69], a complex value of $\kappa = (31 + 0.17\mathrm{i})\,\mathrm{cm}^{-1}$ was obtained from simulations of the realized DFB gratings. However, the small but finite imaginary component of the coupling coefficient is essential for the single-mode operation of the QCL array elements, as it results in favoring of one of the two DFB modes for lasing. The related loss contrast between the two modes is caused by a difference in free-carrier absorption strength in the grating host and cladding layers (see discussion in Section 4.2), where waveguide losses of 8.1 and 7.4 cm^{-1} were calculated for the low- and the high-frequency DFB modes in reference [69], respectively. Without any additional influences on the mode-selection process, this loss difference results in deterministic lasing of the high-frequency DFB mode. However, uncoated device facets significantly influence the lasing mode selection in case of moderate loss contrast between the two DFB modes, as discussed in detail in the following.

In reference [69], our group presented a detailed study of the facet influence on the selection of the lasing mode in a DFB QCL as well as on its output power, in dependence on the grating coupling strength κL. The analysis given in this paper is based on the theoretical treatment of facet effects for diode lasers published in reference [73]. In an ideal DFB laser without any facet influence (e.g. for very long cavities or AR-coated facets), electromagnetic waves travelling through the waveguide experience continuous feedback due to scattering by the periodic index variations, which can be described as coupling between left- and right-travelling waves. Eigenmodes of this system or stationary solutions of the coupled wave equations can be interpreted in terms of fulfilling roundtrip conditions for amplitude and phase for formation of a standing wave. Now, in the case of non-negligible reflections from the QCL facets, these roundtrip conditions are perturbed by the additional left- and right-travelling wave components of the reflected radiation in a way that strongly depends of the phase of these components relative to those of the unperturbed DFB cavity. For a strong influence of the facet reflections, mode-selection phenomena related to coupled cavities like those studied experimentally in reference [74] can occur. The crucial phase relation between the unperturbed DFB wave components and the additional facet reflections depend on the precise position of the facet with respect to the stationary intensity profile of the DFB cavity, which is of the same periodicity as the grating as illustrated in Fig. 2a. The low- and the high-frequency DFB modes, separated by the photonic bandgap as indicated in Fig. 2b, exhibit a shifted intensity profile with respect to each other, and are thus influenced by the presence of facet reflections in different ways. A facet mirror positioned exactly at a field node of one of the two DFB modes and thus suppressing lasing at this mode coincides with a field maximum of the other DFB mode resulting in low associated mirror losses due to constructive interference. As a consequence, facet reflections can favor one mode over the other, and result in lasing of either or both of the two DFB modes, depending on the precise facet position within one grating period.

The influence of the device facet on the properties of a DFB QCL strongly depends on the coupling strength of the grating. As mentioned in Section 4.1., κL determines the longitudinal field distribution inside the laser. For a strong coupling $\kappa L \gg 1$, the lasing modes are confined to the center of the cavity, and the intensity at the device facets is weak. Consequentially, such overcoupled DFB lasers suffer from small slope efficiencies due to the weak outcoupling of radiation. For weakly coupled DFB lasers with $\kappa L \ll 1$, on the other hand, the mode intensity is concentrated close to the device facets, showing a minimum at the center of the cavity [66,69]. As predicted by the simulations in reference [69], the positions of the two facet mirrors strongly influence the DFB device operation in case of weakly and moderately coupled gratings with $\kappa L \sim 1$, assuming uncoated facets with reflectivity of 30%. Lasing at the high-frequency mode, which would be dominant in an unperturbed DFB QCL, can be suppressed in favor of the low-frequency mode due to the facet influence. Figure 2c shows a plot of the simulated total loss difference between the low- and high-frequency DFB mode as a function of the mirror facet positions (or phases) for $\kappa L \sim 4.6$. As seen from the plot, the modelled device is expected to lase on the low-frequency DFB mode in 43% of all cases (positive loss difference values), while the high-frequency mode is selected with a probability of 66% (negative loss difference). The facet position with respect to the DFB grating is not controlled for the array devices presented in reference [69], and the submicrometer precision required for feedback control is in principal difficult to achieve. Furthermore, as the facets of all array elements are defined during one fabrication step by cleaving, and the grating period

© 2015 by WILEY-VCH Verlag GmbH & Co. KGaA, Weinheim

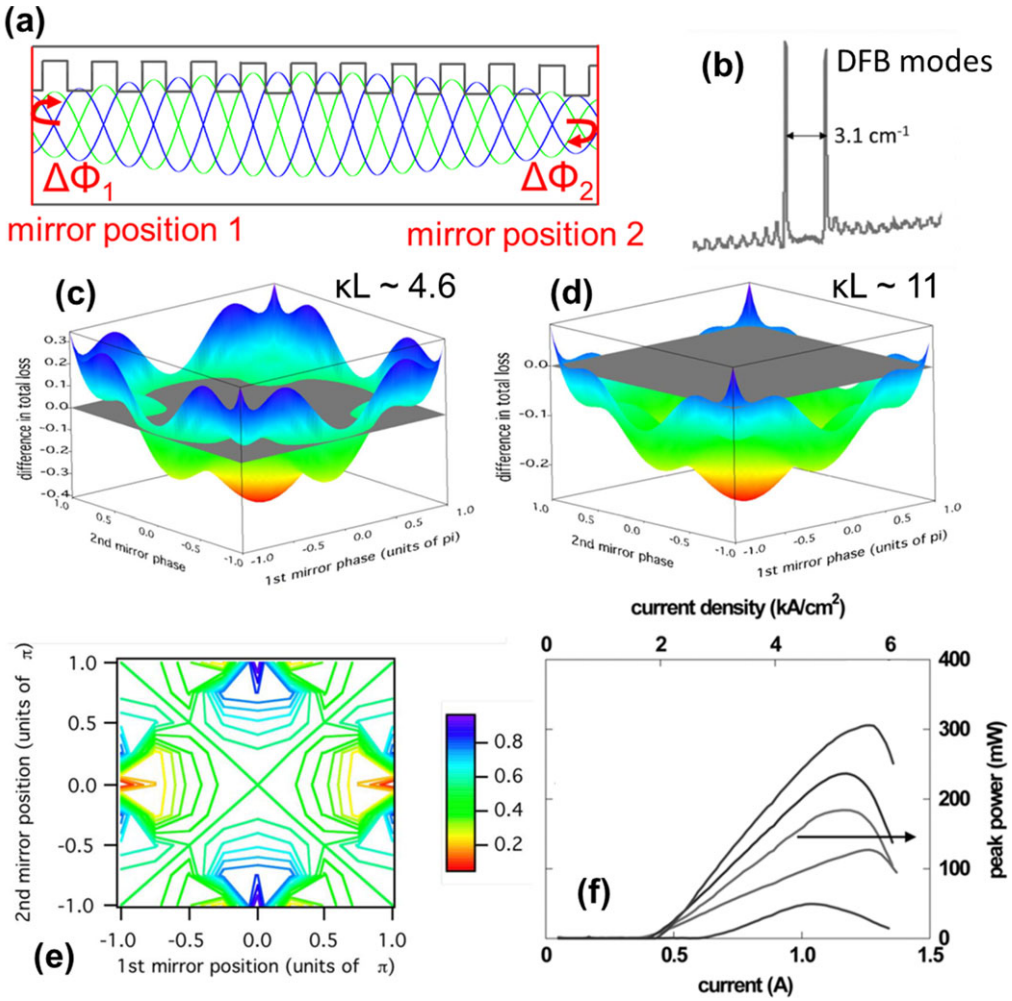

Figure 2 Influence of the device-facet mirrors on the performance of DFB QCLs in an array. (a) Illustration of the dependence of the facet influence on their position relative to the DFB grating. The figure shows a side-view sketch of the DFB waveguide, with overgrown grating and two facet mirrors in red. The radiation reflected by the facet mirrors interferes with the standing waves of the two unperturbed DFB modes (electric-field amplitudes sketched in green and blue), and influences the mode losses depending on the relative phase between the reflection and the unperturbed DFB mode. (b) Electroluminescence spectrum recorded for one of the array elements in reference [69] at a current below threshold, showing the two DFB modes separated by the photonic bandgap. (c) Simulated difference in losses between the low- and high-frequency DFB modes as a function of the two facet positions relative to the DFB grating (expressed in relative phases of the reflected radiation) for moderate coupling ($\kappa L \sim 4.6$). For positive values of the loss difference, lasing on the low-frequency DFB mode is favored, for negative values the high-frequency mode is expected to lase. In the case of moderate coupling, lasing on the low-frequency DFB mode is expected to occur for 43% of the devices in an array with uncontrolled facet positions and no coatings. (d) By increasing the coupling strength to $\kappa L \sim 11$ in overcoupled DFB QCL arrays, the facet influence can be suppressed, achieving negative values of the loss difference for all mirror positions and resulting in deterministic lasing on the high-frequency DFB mode for all of the array elements (see Figs. 1a and b). (e) Simulated influence of the facet-mirror position on the output power ratio between the front and back facet emission for $\kappa L \sim 4.6$. The power ratio is shown as a contour plot in dependence of the two facet positions/phases. (f) Large variation of the slope efficiency resulting from the facet influence on lasing of a moderately coupled DFB QCL array with uncontrolled facet positions and no coatings, where the slope efficiency of the elements spreads over one order of magnitude. (b)–(f) Reproduced with permission [69]. Copyright 2009, IEEE.

varies from element to element, the facet mirror reflections influence each array element *differently*. For a given device with a moderately coupled DFB grating, the selection of either the low- or high-frequency mode for lasing is thus determined by an uncontrolled facet positioning and therefore completely random. For a single QCL device this is not crucial, as a series of devices can be fabricated, tested and then distributed across different applications according to their specific lasing wavelength. However, for a DFB QCL array, lasing at equidistant wavenumbers is desired, not only for reasons of clean and continuous tunability, but also to enable efficient beam combining as discussed

© 2015 by WILEY-VCH Verlag GmbH & Co. KGaA, Weinheim

in the next section. The width of the photonic bandgap and thus the uncertainty in the precise lasing wavelength amounts to about 3 cm^{-1} in case of $\kappa \sim 30$ cm^{-1}, and the wavenumber spacing across the DFB QCL array can thus vary by up to 6 cm^{-1} for the moderately coupled devices discussed in reference [69]. An experimental observation of this random selection of the DFB mode for lasing and the consequential variation in wavenumber spacing in a moderately coupled DFB QCL array designed for equidistant emission wavenumbers was presented in reference [69] alongside the theoretical considerations: Figure 1c shows emission spectra for a DFB QCL array with 32 devices ($\kappa L = 4.6 + 0.025$i) and with two uncoated facets, demonstrating lasing of 18 devices on the high-frequency and 14 on the low-frequency DFB mode. As the photonic bandgap of the presented array has a width of 3.1 cm^{-1} (Fig. 2b), the wavenumber spacing between subsequent array elements deviates from the targeted 2.7 cm^{-1}, amounting 5.8 cm^{-1} in some cases and even changing sign to –0.4 cm^{-1} for others.

Alongside a detailed analysis of the facet-mirror influence on the mode selection in DFB QCLs, two strategies for overcoming these challenges regarding homogeneous performance of index-coupled DFB laser elements in an array are presented in reference [69]. The first method is based on confining the lasing mode intensity distribution to the center of the QCL cavity by realizing overcoupled DFB gratings. The latter is achieved by fabricating long devices, reaching $\kappa L \sim 11$, as already demonstrated in reference [67] and discussed in Section 4.2. Figure 2d shows the simulated loss difference between the two DFB modes for an overcoupled DFB device with $\kappa L = 11 + 0.025$i, where negative values are predicted for the vast majority of facet mirror positions/phases. Thus, as concluded from these simulations, the facet influence on mode selection is negligible for such overcoupled DFB QCL arrays, and all 32 devices of the demonstrated chip lase on the high-frequency mode selected by the charge-carrier-induced losses, as seen in Figs. 1a and b. It should be mentioned that too strong overcoupling has to be avoided, as it reduces the facet-mirror losses compared to the waveguide losses and therefore the slope efficiency and maximum output power of a device. Extreme overcoupling further leads to a pronounced inhomogeneity in the longitudinal field distribution of the laser mode with a strong peak at the center of the device [66], increasing the influence of gain-saturation effects. A thorough choice of the coupling coefficient is therefore crucial for combining high output power with reliable and deterministic single-mode operation. The second, rather straightforward strategy for achieving the latter is to cover the device facets with an AR coating to effectively eliminate the facet-mirror influence. Figure 1d shows emission spectra for each element of a moderately coupled array ($\kappa L = 4.6 + 0.025$i) with an AR coating applied to the front facet [69]. 25 of the devices are lasing on the high-frequency mode, and 6 on the low-frequency side, which is a strong improvement to the 18:14 ratio for the uncoated device of equal coupling. The ratio of 25:6 agrees well with the theoretic prediction. One of the devices showed simultaneous lasing on both sides of the bandgap, a case that can occur at certain positions of the facet mirror. Application of AR coatings on *both* device facets is predicted to achieve deterministic lasing on the high-frequency DFB mode, but would significantly reduce the output power achieved by the array.

All DFB QCL arrays demonstrated in references [67, 69, 70] suffered from a pronounced inhomogeneity of the accessible output power across the array, caused by a large variation in the slope efficiencies from element to element. The latter was attributed to the influence of the device facets on the intensity distribution inside the cavity, where an asymmetric distribution can result in preferential outcoupling of the radiation from one device facet, while the output power from the other facet is weak. A detailed study of this effect was again given in reference [69], and simulation results for the output-power ratio between the front and back facets in dependence on the facet positions are shown in Fig. 2e. Highly asymmetric positioning of the two facets, with one facet positioned in the peak and one in the valley of the etched corrugation, leads to strong asymmetries in the mode intensity distribution along the ridge. As a result, the outcoupled power can be distributed between the two facets as unevenly as 95:5. For single DFB QCL devices, this uneven distribution is an inconvenience rather than a real issue, as the output direction of a device in a system can be freely chosen after testing the power emitted from both facets. However, for an array of QCLs, it is required that all devices emit with comparable intensity in one direction, and the influence of uncoated device facets can result in an inhomogeneous power distribution across the array spectrum. Figure 2f illustrates the experimental observation of this issue for an array of moderately coupled DFB QCLs demonstrated in reference [69], where the light–current characteristics of a few selected devices are shown, exhibiting a strong variation in slope efficiency by one order of magnitude. This slope efficiency variation persisted across all the demonstrated DFB QCL arrays, and crucially limits the output power range achieved by these arrays. However, as shown in Section 7, the addition of integrated power amplifiers in MOPA QCL arrays not only tremendously increases the average output power achieved by the elements, but also strongly reduces the power variation across the array.

To summarize this section, for realizing DFB QCL arrays with deterministic, equidistant wavelength spacing between the elements and a homogeneous achievable output power across the array, a thorough choice of the coupling coefficient and device length and/or the application of AR coatings to one or both laser facets are crucial. As shown in Section 7 discussing the progress on high-power multi-wavelength arrays of single-mode QCLs, the suppression of the influence of device facets on the mode selection becomes even more crucial utilizing power amplification sections in the array, while the facet influence on the output power variation is significantly reduced in such a configuration.

© 2015 by WILEY-VCH Verlag GmbH & Co. KGaA, Weinheim

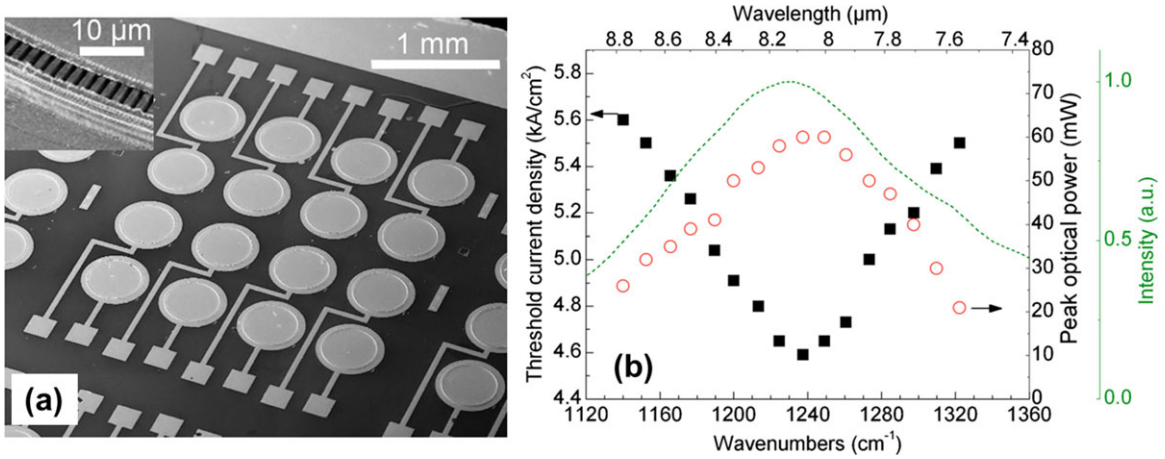

Figure 3 Surface-emitting ring-cavity QCL arrays. (a) Electron micrograph of a two-dimensional array of surface emitting ring-cavity QCLs. The inset shows an image of the employed second-order surface grating. (b) Performance of the ring-cavity QCL elements. Threshold currents, achieved peak power and emission wavenumber are given for each individual device, along with an electroluminescence spectrum of the gain material (green dotted line). (a), (b) Reproduced with permission [75]. Copyright 2011, AIP Publishing LLC.

5. Surface-emitting quantum cascade laser arrays

In contrast to the edge-emitting QCL arrays demonstrated by our group, the group of Gottfried Strasser has reported on a two-dimensional multi-wavelength array of surface emitting ring-cavity QCLs in reference [75]. As shown in Fig. 3a, this array comprises 16 elements arranged in a 4-by-4 grid, fabricated from material based on a continuum-to-bound design [76] with a gain centered around 8.13 μm and featuring a FWHM of 200 cm^{-1}. Wavelength selection and surface emission are achieved by radial second-order Bragg gratings etched 1.9 μm deep into the top cladding, where the grating period was varied from device to device. Each of the ring-cavity DFB QCLs forming the array showed single-mode operation at equidistant wavenumbers over a range of 180 cm^{-1}. An inherent advantage of the ring-cavity configuration is the absence of facets, eliminating the need for strategies to suppress their influence on mode selection and output power. The lack of any facet influence results in a consistent lasing on the antisymmetric mode of the second-order grating for the array elements in reference [75] as well as in a low output power variation between the individual lasers dominated by the fluctuation in the gain spectrum. The latter is evident from a comparison of the fluctuation of the achieved output power of the array elements (red circles in Fig. 3b) with the shape of the gain spectrum (dotted green line). However, ring-cavity QCLs also face a series of disadvantages. Their relatively large footprint (diameter of 400 μm) as well as the two-dimensional structure of the array makes beam combining challenging. And even though they can feature impressively narrow far-field intensity distributions with FWHM values of 3° in both axes [77], their far-field exhibits an intensity minimum in the center, and targeting a center-lobed emission requires the introduction of phase-shift sections. Furthermore, the polarization state of the ring-cavity emission is rather complex, resulting from the azimuthal polarization in the near-field imposed by the grating. Only recently, linearly polarized emission from such a ring-cavity QCL has been demonstrated by utilizing transmission through a wire-grid polarizer fabricated on the bottom surface of the chip substrate [78]. Last but not least, the peak output powers demonstrated for ring cavity DFB QCLs in an array so far have been very limited, with values between 20 and 60 mW achieved in pulsed operation by the array in reference [75], where the low output power was attributed to the losses introduced by the deeply etched grating. Thus, while these two-dimensional arrays show potential for specific applications due to their unique properties, their output power at present limits their application in fields targeted by the high-power arrays on which this review article is focused.

An alternative approach to realizing surface emitting QCL arrays has been very recently demonstrated by the group of Faist in reference [79]. In this work, a multi-wavelength array comprising ten devices with integrated distributed Bragg reflectors for wavelength selection has been realized. Outcoupling of the laser emission is achieved via a dielectric second-order grating in the central section of each array element, fabricated simultaneously with the Bragg gratings for wavelength selection. The demonstrated array features longitudinal single-mode operation at ten different wavelengths between 8.3 μm and 9.7 μm, spanning a wavenumber regime over 175 cm^{-1}. The employed wavelength-selection mechanism enabled reliable lasing at a defect mode in the center of the photonic bandgap of the Bragg reflectors for nine out of ten devices. However, despite a buried heterostructure approach that in principle supports cw operation, the performance of the array was rather modest. Output power values of the individual array elements between 0.7 and 2 mW were reported in pulsed operation and at –20 °C, and the devices suffered from

© 2015 by WILEY-VCH Verlag GmbH & Co. KGaA, Weinheim

high threshold current densities around 5 kA/cm^2. The performance issues were attributed to leakage currents and a low outcoupling efficiency, and the demonstrated surface-emitting array concept requires optimization before competitive figures of merit can be achieved.

6. Wavelength beam combining of the quantum cascade laser array output

For stand-off detection schemes employing EC QCLs, a beam with a diameter of more than a centimeter is aimed at the suspicious substances to analyze, and the backscattered radiation is imaged by a camera. As briefly mentioned in Section 3, commonly employed EC configurations compensate tuning-induced changes in the beam direction and beam walk-off issues, and the illuminated spot maintains its position on the test substance during the tuning process even at distances of several tens of meters. As discussed in the following, means of beam-steering error compensation are also required for multi-wavelength QCL arrays, even though no movable components are involved in contrast to EC QCLs.

The employment of QCLs in spectroscopy systems commonly requires the use of optical components for beam collimation due to the highly divergent output of these devices, with a FWHM angle of typically 60° in the slow axis. The latter is due to the narrow confinement of the optical mode in surface normal direction required to ensure a good overlap with the active material, which is typically only a few micrometers thick. In the simplest configuration, beam collimation is achieved by a lens of small focal length placed in front of the output facet, which generates a parallel beam with roughly the same diameter as the lens. When placing a lens in front of a QCL array, with the central device exactly in the focal point of the lens, the direction of the generated parallel beam varies from array element to element, following $\tan(\Theta) = x_n/f$, where Θ is the pointing angle relative to the emission direction of the center element, f the focal length of the lens, and x_n is the distance of the element from the focal point [80]. For a pitch between the individual lasers of $\Delta x = 75$ μm and $f = 2.5$ cm, this pointing error prevents an overlap between the emission of all array elements already at a distance of one meter from the chip, even though the emission-angle difference between neighboring elements only amounts to a few milliradians (mrad). For beam combining of diode lasers in an array, several methods have been demonstrated [81], among them so-called wavelength beam combining, which is suitable for multi-wavelength arrays such as those discussed in this review.

The first demonstration of wavelength beam combining of a QCL array was reported in reference [80], where a reflection grating was used to correct for the steering error caused by the varying distances of the array elements from the focal point of the collimating lens. The setup for wavelength beam combining is shown in the inset of Fig. 4a and in the photograph of Fig. 4b. The output of the laser array is collimated by a ZnSe lens of 2.5 cm focal length, where the central element of the array is placed at the focal point. The resulting parallel beams hit an aluminum-coated reflection grating with 750 lines/cm and a blaze of 12 μm. Due to the varying beam direction of the individual QCLs, the beam of each element hits the grating at a different angle to its surface normal. According to the grating equation, the output angle Θ_{out} from the grating and the incident angle Θ_n have to fulfill $d\cdot(\sin\Theta_n + \sin\Theta_{\text{out}}) = m\cdot\lambda_n$, where λ_n is the wavelength of the respective array element, and m is the used order of diffraction [80]. In order to achieve successful wavelength beam combining, the equation has to be fulfilled for a fixed output angle by all array elements. Θ_n is given by $\Theta_n = \arctan(x_n/f) + \Theta_g$, with a freely chosen but fixed grating angle Θ_g. For an array with equidistantly spaced emission wavenumbers and a homogeneous spatial distance between the elements, this equation can only be fulfilled in linear approximation, leaving a residual pointing error in the real system. Nevertheless, a reduction in the pointing error from about 80 mrad without a grating down to a maximal error of 2 mrad was achieved for the QCL array demonstrated in reference [82] by using one grating for wavelength beam combining. A plot of the residual errors is given in Fig. 4a. One way to avoid the systematic residual pointing error is to adjust either the wavelength spacing or the pitch between the array elements in order to exactly fulfill the nonlinear grating equation. However, this requires an accurate knowledge of the effective refractive index. Furthermore, temperature tuning of the QCL array would again introduce a residual pointing error, as the grating equation can be fulfilled at only one set of wavenumbers for a fixed spacing of the QCL elements. As an alternative to engineering the wavenumber/pitch configuration of each array element, the authors in reference [82] present a wavelength beam combining scheme employing two gratings, were an excellent reduction of the residual pointing error down to 0.2 mrad was achieved for an array with equal spatial and wavenumber spacing between the elements. In the setup shown in Fig. 4c, the first grating overcompensates the pointing error of the collimated QCL beams, while the second grating simultaneously corrects for this overcompensation and for the residual pointing error introduced by the nonlinearity of the grating equation. In the particular configuration demonstrated in reference [82], the QCL output was collimated by a combination of an array of integrated Ge microlenses (75 μm focal length) and a ZnSe lens of 20 mm focal length, and then combined by two gratings of 1000 and 500 lines/cm, respectively. Figure 4d shows the residual pointing error between the QCL array elements, demonstrating an excellent collinearity between the individual beams. As discussed in reference [82], the drawback of the dual-grating-based wavelength beam combining scheme is its relatively low beam combining efficiency of 30%, defined as the ratio between the power of the system output beam and the QCL emission power measured directly after the microlens. The reason for the low efficiency is the mismatch between the QCL polarization and the orientation of the grating lines, and an enhancement of the combining efficiency to 90% can be expected

© 2015 by WILEY-VCH Verlag GmbH & Co. KGaA, Weinheim

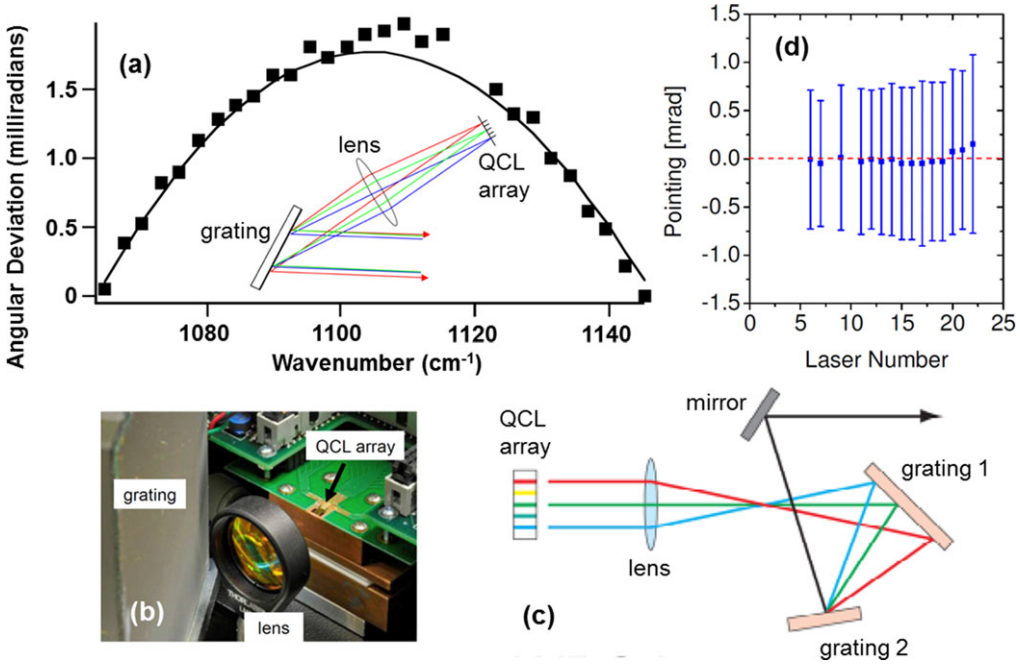

Figure 4 Wavelength beam combining. (a) The relative pointing error between the individual collimated beams of a DFB QCL array after wavelength beam combining with a single grating. The residual pointing error is due to the equidistant spatial and wavenumber spacing between the 32 array elements and the nonlinear nature of the grating equation. The setup for single-grating beam combining is shown in the inset and in the photograph of (b). (c) The schematics show a two-grating beam-combining setup for further reducing the residual pointing error. The first grating overcompensates the initial pointing error, while the second grating corrects both this overcompensation and the error caused the linear approximation of the grating equation. (d) Relative pointing errors below 0.2 mrad between the DFB QCL array elements were achieved in the two-grating configuration. The squares indicate the relative pointing direction of the far-field intensity maximum, while the vertical bars illustrate the $1/e^2$ width of the individual beams, indicating an excellent overlap between the collimated beams. (a), (b) Reproduced with permission [80]. Copyright 2009, SPIE. (c), (d) Reproduced with permission [82]. Copyright 2011, Optical Society of America.

for an optimized system using a half-wave-plate to rotate the polarization of the QCL output. It should be pointed out that even though wavelength beam combining requires external optical components as a means of eliminating beam steering of the collimated array output during wavelength tuning, the combined system is still free of any moving elements, robust and of low maintenance requirements.

7. Master-oscillator power-amplifier QCL arrays

7.1. MOPA QCLs

As discussed in Section 4, while DFB QCLs as building blocks of multi-wavelength arrays are suitable for spectroscopy systems with relaxed power requirements, their choice as array elements has so far limited the peak output power by such an array. In order to target applications like stand-off detection, a single-mode QCL device reliably delivering high output powers at a good beam quality is needed as a basis element. Even a stable multi-lobed far-field intensity distribution is unacceptable for stand-off applications, as the pointing directions of the intensity peaks would vary from device to device, and wavelength beam combining would be impossible to achieve. Thus, a single lobed far-field intensity distribution in facet normal direction of all array elements is a crucial requirement for a number of spectroscopy and sensing applications, in combination with stringent power requirements for sensitive and reliable detection. Both can be addressed by employing MOPA QCLs as array elements.

QCLs are generally prone to lasing at higher-order transverse modes due to spatial hole burning, which in turn results in multi-lobed and often strongly current-dependent far-field intensity distributions. Achieving a clean, single-lobed far-field distribution due to exclusive lasing at the fundamental TM_{00} mode requires the introduction of losses for higher-order transverse modes. The latter is commonly achieved by keeping the ridge width of QCLs narrow and thus weakening the confinement of higher-order transverse modes, which also limits the output power available from conventional single-mode DFBs. Several schemes have been pursued in order to overcome this trade-off between output power and beam quality. Photonic crystal QCLs employ distributed feedback for both longitudinal and transverse mode control. However, their design and fabrication is complex and they are susceptible to longitudinal multi-mode operation at high currents [14]. The broad-area angled

© 2015 by WILEY-VCH Verlag GmbH & Co. KGaA, Weinheim

cavity QCLs in so-called β-DFB configuration demonstrated in reference [13] require relatively high currents beyond 40 A for achieving single-mode peak powers of around 3 W, and would require a large pitch when forming an array due to their large facet width of more than 200 μm. One concept, which meets the requirements for providing high output powers at a good beam quality and single-mode operation in an array is that of master-oscillator power-amplifiers. The principle is based on generating a single longitudinal and transverse mode in a low-power laser device, and coupling this mode into a single-pass amplifier, where it is amplified while maintaining its spectral purity as well as its mode profile. MOPAs have been successfully realized in a variety of systems and geometries, and a monolithic MOPA diode laser was demonstrated in 1990 [83]. Two years later, the first monolithic MOPA semiconductor laser with a tapered (flared) amplifier was realized [84], a geometry that enabled achieving 10 W of cw power in a single-lobed diffraction-limited beam from a semiconductor laser in 2007 [85]. The first monolithic QCL device in MOPA configuration was reported in reference [86], capable of 0.5 W of output power at 80 K. In 2010, our group finally reported on the first high-power operation of a monolithic MOPA QCL device, reaching peak powers of 1.5 W in both longitudinal and transverse single-mode operation and at room temperature [87]. As the device layout forms the basis of the high-power multi-wavelength MOPA QCL arrays reviewed in this section, the operation of the device reported in reference [87] is briefly discussed in the following.

MOPAs are two-section devices, comprising a single-mode seed section (master oscillator, MO), and a power-amplifier (PA). The MO section is required to lase at a single longitudinal and transverse mode, where moderate powers are sufficient. Narrow DFB ridges are an obvious choice for the seed section and have been employed for all of the MOPA QCLs demonstrated up to now. In a monolithic device, both the seed and amplifier sections are fabricated from the same material. Under ideal operation, the latter acts as a single-pass PA in travelling-wave configuration, meaning that radiation fed into the PA section from the input side is gaining in power while propagating along this segment, maintaining its original modal composition and spectral properties. The layout of the MOPA QCL demonstrated in reference [87] is illustrated in Fig. 5a, including a narrow MO DFB ridge that is on one side connected to a tapered PA section. Though it seems to be an intuitive choice, the reason for the tapered geometry of the PA will be discussed in the following.

Proper operation of the PA section has two crucial requirements: First, in order to guarantee spectral purity, the activity of this segment has to be strictly limited to amplification of the seeded mode, and self-lasing of the PA inevitably leading to a multi-wavelength output has to be suppressed. To prevent the PA section from forming a cavity for self-lasing, feedback from the PA output facet has to be eliminated. While different concepts for the latter have been demonstrated [86], the preferred means is achieving a high outcoupling efficiency by the application of a high-quality AR coating [87]. As the second crucial requirement, the seeded TM_{00} mode has to traverse the PA without scattering into higher-order transverse modes, which guarantees a single-lobed far-field intensity distribution of the MOPA output beam. This requirement puts restrictions on the geometry of the PA. A rapid change of the cross section of the travelling-wave amplifier along the propagation axis would be accompanied by a rapid change in the profile of its eigenmodes, and scattering into higher-order modes during propagation would occur. Only a slow, gradual change of the waveguide cross section allows a continuous propagation of the electromagnetic wave without scattering into higher-order modes and, in the tapered geometry shown in Fig. 5a, a so-called adiabatic expansion of the seeded TM_{00} mode. The taper half-angle of the PA in reference [87] is 1°, and the adiabatic spreading of the TM_{00} mode in the amplifier section is illustrated by a contour plot of the simulated intensity distribution in the PA, as shown in Fig. 5a, resulting from finite-difference time-domain (FDTD) calculations. As seen from the plot, the mode continuously gains in intensity and expands in cross section, but its intensity distribution stays perfectly single-lobed.

The tapered geometry for the amplifier section aims at mitigating gain-saturation effects in the QCL material. Gain saturation is intensity dependent and sets in as soon as stimulated emission contributes significantly to the depopulation of the excited state of the optical transition. In case of lasing, the gain is clamped at the threshold gain value as soon as lasing sets in, and gain clamping is a direct manifestation of gain saturation. In a QCL-based amplifier in a single-pass configuration, lasing does not occur due to the lack of feedback, and the amount of gain saturation depends on the highly inhomogeneous intensity distribution along the amplifier (see Fig. 5a). The tapered PA geometry allows spreading of the mode over a larger cross-sectional area and thus reduces the mode intensity and gain saturation, supporting high output powers. For MOPA QCL devices with a straight and narrow PA section, the highest peak-power values reported up to now for single-mode operation are just below 1 W [88]. In contrast, the tapered amplifier geometry of the arrays reviewed in Section 7.2. enables achieving peak powers of several Watts up to 10 W. The detailed choice of the PA length and taper angle depends on a series of parameters from material properties to the specific requirements of the targeted application in terms of, e.g., accessible driving current range, footprint area and array pitch, and the optimization of the MOPA layout requires a detailed device simulation due to the inhomogeneous current-density distribution and heating effects. With increasing amplifier length, lateral temperature and refractive-index gradients gain an influence on the beam quality, and have been reported to lead to filament formation and beam instabilities in tapered semiconductor amplifiers [89]. It should be mentioned that tapering of an amplifier further introduces a significant astigmatism in the output beam of the device. However, the latter can be corrected by using a cylindrical lens in the external collimating or beam combining setup (see Sections 6 and 9.2.).

© 2015 by WILEY-VCH Verlag GmbH & Co. KGaA, Weinheim

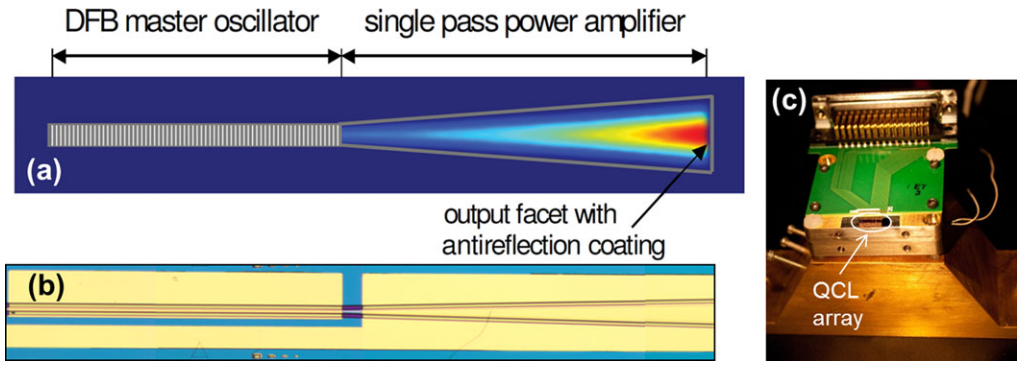

Figure 5 MOPA QCL layout and array packaging. (a) Basic layout of a monolithic MOPA QCL, comprising a DFB QCL as single-mode master oscillator and a tapered amplifier with AR-coated output facet. The contour plot shows the adiabatic spreading of the TM_{00} mode seeded by the DFB section. While traversing the single-pass amplifier, the mode grows in power and maintains its spectral purity and beam quality. The taper half-angle of 1° reduces gain-saturation effects. (b) Top-view image of an element of the MOPA QCL array. Note the separated top metallization of the two sections, allowing independent driving at different current densities to prevent self-lasing of the PA section. (c) Photograph of the packaged MOPA QCL array, mounted on a thermoelectrically cooled copper heat sink. (a) Reproduced with permission [87]. Copyright 2011, Optical Society of America.

7.2. High-power MOPA QCL arrays: Design and performance

The high-power multi-wavelength MOPA QCL arrays presented in reference [90] and [91] were based on a broadband bound-to-continuum design [37], where the material was grown on a conducting InP substrate by organometallic vapor phase epitaxy (OMVPE). The layout of the arrays was similar to that in reference [87], with a taper half-angle slightly increased to 1.3° and a 2-mm long PA section. A top-view image of the layout of an array element is shown in Fig. 5b. The first report on a MOPA QCL array in reference [90] presented a MO section with a more complex DFB grating approach for reducing the influence of the device back facets. However, as this first-generation array was outperformed by an array of a more simplified grating design [91], this article will first review the straightforward approach of a simple DFB QCL as seed section in a MOPA array, and then discuss an alternative design aiming at improved mode control and its shortcomings.

The MOPA QCL array demonstrated in reference [91] comprises 16 elements, each featuring a 13-μm wide and 2-mm long DFB MO section with a 250-nm deep first-order grating etched into the GaInAs host layer and overgrown by InP. The DFB gratings of the MO sections showed a moderate coupling strength of $\kappa L \sim 3$. Varying the grating period from device to device between 1.44 and 1.55 μm allowed single-mode seeding at a different wavelength for each array element. The output facet of the individual MOPA QCLs was 110 μm wide, and the arrays featured a large pitch of roughly 500 μm. It should be pointed out, however, that the large pitch size was merely chosen to facilitate convenient bonding of the individual MOPAs, and that close packing of the elements is feasible.

As discussed above, one of the key requirements for proper MOPA operation is the suppression of self-lasing in the PA section. As a means of reducing the feedback from the front facet of the devices, an AR coating was applied to the MOPA QCL arrays. The coating was composed of 842 nm of ZnS (refractive index of 2.2) and 1280 nm of YF_3 (refractive index of 1.415), where the coating quality is crucial for achieving single-mode emission of the MOPA devices up to high currents and output powers. However, even though the self-lasing threshold of the PA was drastically increased by applying an AR coating, self-lasing still occurred in the devices presented in reference [91] at high amplifier currents. Thus, in order to keep the PA current density below its self-lasing threshold and simultaneously drive the MO section close to its rollover point, the MO and PA sections of MOPA QCLs were electronically separated and can be driven independently. The latter was achieved by introducing a 100-μm wide gap in the top metallization (see Fig. 5b), and separate bonding of the sections. The packaging of the MOPA QCL arrays reported by our group is shown in Fig. 5c. Due to the fact that MOPAs are two-section, three-terminal devices, MOPA arrays require more complex driving solutions involving two separate pulse generators for independent driving. However, the more sophisticated device layout and driving configuration also increases the number of parameters for customizing and tuning of the device performance and thus the flexibility of the array, and, e.g., local temperature tuning of the DFB section by a dc current in combination with a purely pulsed driving of the PA section can be envisioned.

The high-power MOPA QCL array reported in reference [91] is capable of delivering impressive peak output powers between 2.7 W and 10 W in single-mode operation at 14 different wavelengths (two array elements were inoperable). The devices were driven at a heat sink temperature of 18°C and at duty cycles between 0.025 and 0.1%. Figure 6 presents a logarithmic plot of the normalized emission spectra at the respective maximum achievable peak power for single-mode operation for the elements of the MOPA array in reference [91], showing that all of the devices feature a SMSR of at least 20 dB. Remarkably, the variation of the available single-mode peak power across the array

© 2015 by WILEY-VCH Verlag GmbH & Co. KGaA, Weinheim

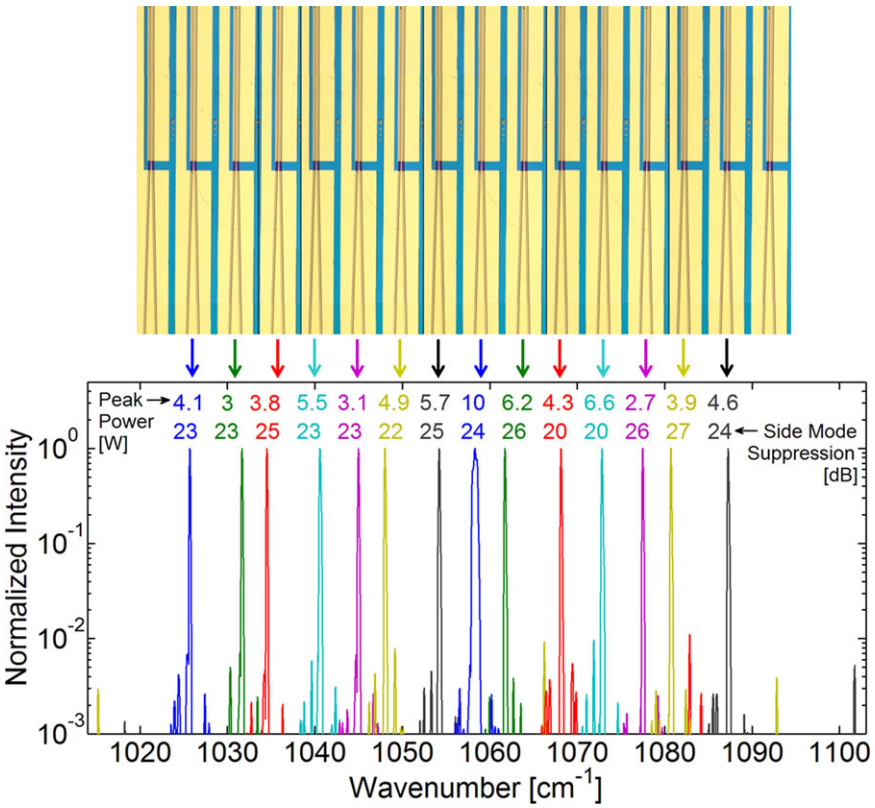

Figure 6 MOPA QCL array performance. The top image shows the layout of the 16-element array, while the achieved single-mode peak power of each element is listed directly below. The MOPA QCL array is capable of single-mode operation (SMSR ≥ 20 dB) with peak-power values between 2.7 and 10 W at 14 different wavelengths, as demonstrated by the normalized spectra shown in the logarithmic plot for each element. All data was acquired at room temperature and pulsed operation.

between 2.7 and 10 W is far less pronounced than for the DFB QCL arrays reported in references [67, 69, 70], where the power values varied by a factor of nearly 10. As the coupling strength of the DFB gratings of the presented MOPA arrays is comparable to that of the moderately coupled DFB arrays in reference [69], a significant variation of the slope efficiency of the seeded power from the DFB section has to be expected due to the influence of the MO back facet (see Section 4.3. and [69]). The significantly more homogeneous output power range for MOPA QCL arrays as compared to DFB QCL arrays can be attributed to a homogenizing effect of the gain saturation in the PA section, as discussed in the following.

The onset of significant gain saturation in the PA was observed despite the finite tapering angle of the amplifier for the arrays in reference [91]. For conventional QCL devices, the output power typically increases linearly with the applied current above threshold due to the strong influence of gain saturation in the cavity. On the other hand, in an optical amplifier with negligible gain saturation, the output power increases exponentially with the driving current, following $P_{\mathrm{out}} = P_{\mathrm{in}} \cdot \exp[-\alpha_{\mathrm{w}} + g{\cdot}\Gamma{\cdot}(j - j_{\mathrm{trans}}){\cdot}d]$, where P_{in} is the input power from the DFB section, α_{w} are the waveguide losses, d is the amplifier length, j the PA current density, j_{trans} the transparency current density of the PA and $g{\cdot}\Gamma$ the (unsaturated) modal gain coefficient [91]. Gain saturation in an optical amplifier is negligible for a small input power P_{in} and short amplifiers. Figure 7a presents a logarithmic plot of the output-power/PA-current characteristics for one of the elements of the array in reference [91] at a series of different MO currents, clearly showing an exponential dependence for low PA and MO currents (the latter equivalent to low input powers), as highlighted by the dotted lines. In this exponential regime, the seeded mode traverses the PA section without inducing significant gain saturation. As the PA current is increased, the intensity gained by amplification of the seeded mode grows strong enough to induce significant gain saturation, increasing towards the end of the amplifier. As the currents are further increased, the onset position of significant gain saturation shifts closer to the MO section, resulting in the subexponential characteristics observed in Fig. 7a for high PA and MO currents. While gain saturation reduces the amplification factor achieved in the PA, it also exerts a homogenizing effect on the output power. This becomes evident, when considering the range of output power variation for a series of different input powers in Fig. 7a. At a PA current of 1 A (low gain saturation), the output power spreads across one order of magnitude, from about 60 mW at an MO current of 1 A to 500 mW at 2.3 A. In contrast, at high PA currents above 6 A (strong gain saturation), the output power spread (from 3.5 to 7 W) is reduced to a factor of two for the same range of input powers. The reason for this reduction in output-power variation with rising PA current is that the overall amplification factor of the PA section reduces with increasing input power due to gain saturation at high PA currents. A gain-saturated amplifier thus compensates input-power variations and exerts a homogenizing effect on the output power. As a consequence, the MO slope efficiencies at a fixed, high PA current vary only slightly across the MOPA

© 2015 by WILEY-VCH Verlag GmbH & Co. KGaA, Weinheim

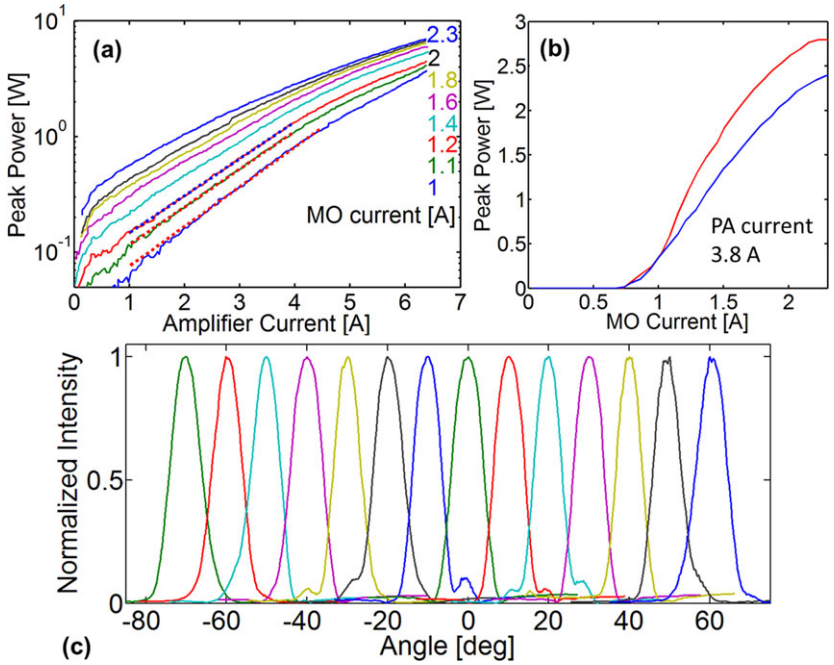

Figure 7 MOPA QCL array light–current and far-field characteristics. (a) Dependence of the output power on the PA current for a series of MO currents in a logarithmic plot for one of the MOPA elements, exhibiting characteristic amplifier behavior. The dotted lines indicate the regime of minor gain-saturation effects, where an exponential dependence is observed. At high PA and MO currents, significant gain saturation is indicated by the flattening of the characteristics. (b) Dependence of the output power on the MO current for a fixed PA current of 3.8 A. The blue and the red curves show the characteristics for the array element with the lowest and highest (amplified) slope efficiency, respectively. (c) Angular far-field intensity distribution of the MOPA QCL array elements in the chip plane at maximum peak power for single-mode operation, demonstrating the excellent beam quality of the array. The individual angular distributions have been offset horizontally for a clear display. (c) Reproduced with permission [91]. Copyright 2013, Optical Society of America.

QCL array demonstrated in reference [91], with values between 2 and 3 W/A (including the fixed PA amplification factor) at a PA current of 3.8 A, as seen in Fig. 7b. Thus, MOPA arrays can be expected to generally show a more homogeneous performance in terms of output power and (amplified) MO slope efficiencies than DFB QCL arrays suffering from the facet influence on the performance.

In addition to tremendously outperforming the DFB QCL arrays in reference [67, 70] both in achieved power levels and homogeneity of the output power across the elements, the MOPA QCL arrays demonstrated in reference [91] feature a significantly reduced inplane divergence of the device emission and excellent beam quality of its elements. The reduction in inplane divergence is due to the large width of the PA output facets of 110 μm in combination with a conservation of the mode profile during amplification. The far-field intensity distributions in the chip plane are presented in Fig. 7c illustrating the beam quality of all array elements at their maximum peak power. A single-lobed intensity distribution with a narrow average inplane FWHM angle of 7.8° indicates adiabatic spreading of the seeded TM_{00} mode during amplification. Only minor side lobes are observed for some of the elements, with no expected significance for collimation, beam combining and performance in stand-off systems. In contrast to the inplane intensity distribution, the divergence of the MOPA output beams in the slow axis is high with FWHM angles around 60°, which is typical of QCLs due to the narrow mode confinement in surface normal direction. Conventionally, the strong resulting divergence in this direction is addressed by external collimation optics. However, the integration of plasmonic collimators into the facet of QCL devices has been demonstrated [7], paving the way to highly collimated emission from a monolithic QCL source. Very recently, this concept has been applied to high-power, broad-area QCLs [92], and the integration of plasmonic collimators into the front facet of future MOPA QCL arrays can be envisioned.

7.3. High-power MOPA QCL array: Device-facet influence

As discussed in the previous section, the MO slope efficiencies at a fixed PA current vary by less than a factor of two across the MOPA array. In contrast, the maximum power values for single-mode operation given in Fig. 6 spread by a factor of 3.7. This is due to the fact that these peak-power values are not limited by the slope efficiencies, threshold currents and rollover points of the respective DFB sections, but by the onset of multi-mode operation at high driving currents. The array reported in reference [91] was characterized by gradually increasing both the MO and PA currents up to a point, where single-mode operation was compromised due to lasing at additional modes, determining a maximum power level for single-mode operation. Thus, the power values given in Fig. 7 have been acquired for different MO/PA current combinations.

In reference [91], two different scenarios for the onset of multi-mode operation were distinguished for the MOPA array elements. For all but one of the elements, an increase of the PA current beyond a certain value resulted in self-lasing of the amplifier due to the finite residual reflectivity of the AR coated front facet. The second scenario for the onset of multi-mode operation is relevant at high MO currents. While several MO sections are capable of single-mode seeding for currents close to their rollover point (current for maximum power), for some DFB elements the accessible current range for single-mode operation is limited due to the onset of multi-mode seeding. The multi-mode

© 2015 by WILEY-VCH Verlag GmbH & Co. KGaA, Weinheim

operation of some MOs for currents approaching the rollover point relates to the influence of feedback from the device facets on mode selection, in analogy to the facet-mirror influence on the operation of conventional DFB QCLs as studied in reference [69] and reviewed in Section 4.3. For several devices of the array in reference [91], multi-mode operation was clearly identified as lasing on both sides of the photonic bandgap. The DFB sections of the MOPA array experience *amplified* feedback from the front facet, and a stronger influence can be expected for a given residual front mirror reflectivity as compared to the DFB arrays with an AR-coated front facet studied in reference [69].

The influence of the device facets on the mode selection in the DFB section is also evident from the single-mode emission spectra shown in Fig. 6. While operation of the array at 16 equidistant wavenumbers was targeted, the observed wavenumber spacing between neighboring elements varies and is either around 4.6 cm^{-1}, 3.1 cm^{-1} or 6.1 cm^{-1}. These numbers are equivalent to the targeted Bragg wavenumber spacing and the target spacing reduced or increased by the width of the photonic bandgap, respectively. Figure 6 shows that nine of the MO sections operate on the high-frequency DFB mode, and five on the low-frequency mode, a ratio slightly lower than the 75:25 reported in reference [69] for a DFB QCL array with higher coupling strength.

For future arrays, a reduction in facet influence can target both the stability of single-mode operation to further push the power range accessible across the array and an equidistant wavenumber spacing for efficient beam combining. This can be addressed either by improving the front facet AR coating, by realizing overcoupled DFB MO sections, or by applying an AR coating to the back facet of future MOPA QCL arrays. An alternative approach for achieving equidistant wavenumber spacing due to deterministic lasing on one particular cavity mode was studied in reference [90], as discussed in the following.

7.4. MOPA QCL array with quarter-wave-shifted DFB sections

In an attempt to achieve more deterministic mode selection in a MOPA array without significantly changing the fabrication, size and driving conditions of the chip, a quarter-wave shift (QWS) was introduced into the DFB gratings of the MOPA array presented in reference [90]. The layout of this array, which was fabricated from the same material as the array in reference [91], is shown in the inset of Fig. 8. While the principal geometry of the MOPA elements in references [90, 91] are equivalent, the latter features an unpumped segment in the MO section in addition to the QWS DFB grating. Both design variations introduced in reference [90] aim at reducing the influence of the device facets on mode selection: The unpumped segment next to the device back facet, realized by a gap in the top metallization, is expected to reduce the feedback from the back facet mirror by absorbing the reflected radiation. The QWS in the DFB grating creates a defect state in the photonic bandgap, and the associated mode is spatially localized around the position of the QWS. Due to the stronger localization at the center of the DFB section, the outcoupling efficiency of the defect mode is lower, and the associated lower losses are expected to result in preferential lasing. The problem of device-facet influence on DFB operation has been known to the semiconductor laser community for a very long time, and the concept of QWSs for achieving deterministic lasing at the defect mode in the center of the photonic bandgap has been studied theoretically and experimentally for diode lasers [93–95].

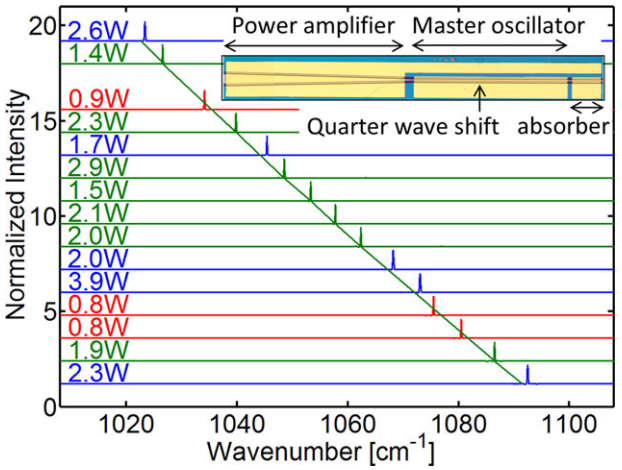

Figure 8 MOPA QCL array with quarter-wave-shifted DFB gratings. For each operative array element, the emission spectrum at maximum single-mode peak power is shown together with the achieved peak-power value. The diagonal green line indicates the Bragg wavenumber of each DFB section, showing that seven array elements lase on the central defect mode associated with the QWS (green spectra), while three operate on the low-frequency (red spectra) and five on the high-frequency DFB modes (blue spectra). The inset shows a top view of one of the 16 array elements, where the position of the quarter-wave shift introduced in the MO section is indicated by an arrow.

Figure 8 presents emission spectra for the MOPA QCL array with QWS demonstrated in reference [90]. In the plot, the spectrum for each array element at its maximum single-mode power is presented, with a diagonal line indicating the spectral position of the defect state mode for each DFB section. Lasing on the latter was observed for seven of 15 array elements, while five MOPAs lase on the high- and three on the low-frequency DFB modes. Thus, while lasing in the center of the photonic bandgap was facilitated for half of the array elements, deterministic lasing at a specific design wavenumber could not be achieved for the QWS MOPA elements. Furthermore, the QWS introduced into the DFB section increased the facet influence on the MOPA performance, and the accessible power values for single-mode operation were far below those of the MOPA QCL array based on conventional DFB sections. The QWS array achieved single-mode peak powers between 0.8 W

© 2015 by WILEY-VCH Verlag GmbH & Co. KGaA, Weinheim

and 3.9 W, where the reduced power values as compared to the array with a straightforward DFB design were caused by multi-mode operation at high PA currents due to simultaneous lasing on the defect mode and one of the DFB modes. As probable cause for the instability of single-mode operation the authors again named the influence of the amplified feedback from the MOPA front facet.

To conclude this section, MOPA QCL arrays achieve impressive performance characteristics, with single-mode peak-power values of several watts across the entire array spectrum, and an excellent beam quality with a narrow, single-lobed intensity distribution in the chip plane. They offer an increased design freedom over common DFB QCL arrays due to the interplay of two components addressing different performance parameters, with a MO selecting the wavelength of emission and a PA scaling the available output power. Due to gain-saturation effects, the output power achieved by the individual elements is more homogeneous across the array than for DFB QCL arrays. With their high peak powers up to 10 W, their superior beam quality, their electrical means of wavelength tuning and independence of mechanical components and their compact dimensions, MOPA QCL arrays are highly suited as a robust, powerful and tunable mid-infrared source for spectroscopy and stand-off detection systems.

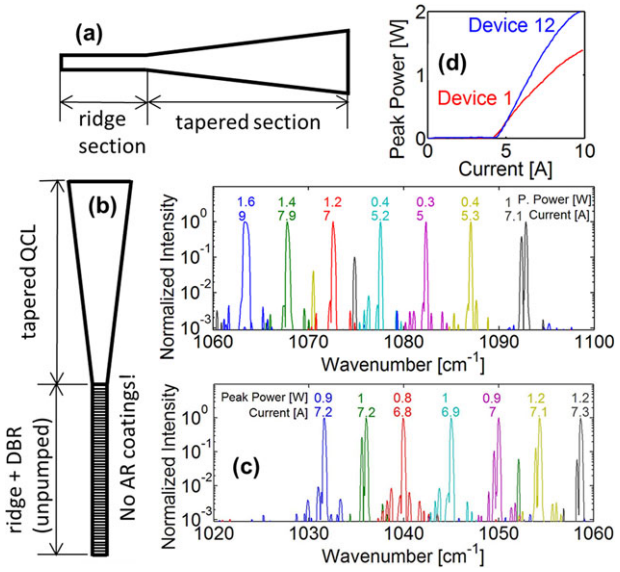

Figure 9 DBR/tapered-oscillator QCLs. (a) Basic layout of a conventional multi-mode tapered semiconductor laser, comprising a narrow ridge section for transverse mode filtering and a tapered broad-area section. (b) Layout of a single-mode tapered QCL, with integrated DBR for longitudinal mode filtering in the ridge section and a tapered cavity. (c) Logarithmic plot of the normalized spectra for 14 DBR/TO QCLs on a chip, each emitting at a different wavelength, together with the corresponding peak-power values and driving currents. For nine of the devices, single-mode operation at peak powers between 0.3 and 1.6 W was achieved at room temperature and pulsed operation. (d) Light–current characteristics for the DBR/TO QCLs with highest and lowest slope efficiency on the chip. (c), (d) Reproduced with permission [99]. Copyright 2013, AIP Publishing LLC.

8. Single-mode tapered QCLs

MOPA QCL arrays are based on two-section devices requiring three terminals for operation. The more advanced driving solutions for MOPA operation might unnecessarily increase the costs and complexity of spectroscopy systems with moderate power requirements. For applications requiring higher power than delivered by DFB QCL arrays, but preferring two-terminal devices for convenient operation, broad-area devices of a tapered geometry are a promising alternative as elements in a multi-wavelength array. The tapered ridge geometry is a means of improving the beam quality of broad-area devices, which in the case of a conventional rectangular layout suffer from lasing at higher-order transverse modes and a consequential multi-lobed far-field intensity distribution. A tapered ridge design for ensuring exclusive lasing on the fundamental TM_{00} mode has been successfully applied to diode lasers for some time, and a review of tapered diode lasers and amplifiers can be found in reference [89]. The basic layout of a tapered semiconductor laser, whether in gain-guided or index-guided configuration, is illustrated in Fig. 9a. The device geometry comprises two segments, a broad-area tapered section and a narrow rectangular ridge. Both facets of the device can be left uncoated, as they are required to form a cavity. For a properly designed tapered laser, the TM_{00} mode is compressed and expands adiabatically during its roundtrip in the cavity, while a dominant fraction of the roundtrip gain is provided in the broad tapered segment due to the spreading of the mode over a larger cross-sectional area. Higher-order transverse modes experience strong losses in the narrow, straight ridge section, and lasing on these modes is consequentially suppressed. The narrow segment thus acts as transverse mode filter, and a high beam quality due to exclusive lasing on the TM_{00} mode can be achieved.

The first demonstration of a tapered QCL was reported in reference [96], and recently our group has realized a high-power, high-brightness tapered QCL achieving peak powers of up to 2.4 W in pulsed operation [97]. 6 W of peak power were reported for next-generation devices fabricated from a different material and with an optimized low-reflectivity coating on the output facet in reference [92]. All of these tapered QCLs were based on a Fabry–Perot cavity and showed lasing at multiple longitudinal modes. In reference [98] the realization of a single-mode tapered diode laser with integrated distributed Bragg reflector (DBR) for wavelength selection was reported, demonstrating the feasibility of both transverse and longitudinal mode filtering by the narrow ridge section of a tapered laser.

In 2013, our group realized the first single-mode tapered QCL based on the integration of a DBR into the narrow ridge section employed for transverse mode filtering [99]. The layout of the demonstrated devices is shown in Fig. 9b. As the design requirements of adiabatic mode expansion in the tapered section and the introduction of high losses for

© 2015 by WILEY-VCH Verlag GmbH & Co. KGaA, Weinheim

higher-order transverse modes in the straight section are basically identical to those for a MOPA device of comparable dimensions, the layout of the so-called DBR/tapered oscillator (DBR/TO) QCLs is equivalent to that of the MOPA QCLs in reference [91]. One essential difference between MOPA and DBR/TO QCLs is that the latter do not require the application of an AR coating, as the tapered section has to form a cavity. While for tapered lasers in the Fabry–Perot configuration the tapered and the straight section are pumped at equal current densities, this is not feasible for DBR/TO devices, as in this case both sections would lase at different longitudinal modes: The DBR section would operate as a DFB cavity and lase on one of the DFB modes, and the tapered segment would additionally lase within the photonic bandgap, resulting in multi-mode operation of the device. Driving of the two sections at different current densities is possible, but would again require three terminals for operation. In reference [99], the authors demonstrated that an unpumped straight DBR section provides sufficient feedback for high-power operation of a DBR/TO QCL, enabling the realization of a single-mode broad-area QCL while preserving the advantage of two-terminal driving.

The DBR/TO QCLs presented in reference [99] were based on the same material as the MOPA arrays in reference [91], with 16 devices on a chip, each featuring a buried first-order grating of varying period as a DBR back mirror. The latter was integrated in a 2-mm long and 13-μm wide ridge. As shown in Fig. 9c, lasing at 14 different wavelengths was demonstrated (two devices were inoperable), where 9 of these 14 devices were capable of single-mode operation (SMSR $>$ 20 dB) up to the current and peak-power values listed above the respective spectrum. The peak-power values accessible for single-mode operation ranged from 0.3 to 1.6 W in pulsed operation. In multi-mode operation, all of the 14 devices on the chip reached power values between 1.4 and 2 W, as illustrated by the light–current characteristics in Fig. 9d, shown for the devices with the lowest and the highest slope efficiencies on the chip. In addition to the selection of the longitudinal mode for lasing due to the wavelength-dependent feedback from the DBR, the efficient operation of the narrow ridge section as a transverse mode filter was demonstrated: All of the DBR/TO devices on the realized chip exhibited an excellent beam quality, with a narrow, single-lobed far-field intensity distributions in the chip plane and a FWHM angle around 7°, indicating pure TM_{00} operation and effective suppression of lasing on higher-order transverse modes.

While the chip presented in reference [99] might not fully qualify as a tunable single-mode source due to the fact that five of the devices did not achieve a SMSR of 20 dB, it clearly demonstrates the potential of DBR/TO QCLs as building blocks for arrays aimed at spectroscopy applications of moderate power requirements (see Section 9.2.). The broad-area devices are capable of peak-power values in excess of those provided by narrow-ridge DFB QCLs and feature a significantly narrower inplane far-field intensity distribution. The reason for the multi-mode lasing compromising proper array operation for five devices was attributed to the large width of the photonic bandgap (1.5 cm^{-1}) of the gratings, which were not optimized for functioning as a DBR mirror with a narrow stopband. By matching the width of the stopband to the free spectral range of the cavity formed by the device front facet and the DBR back mirror in future DBR/TO arrays, reliable single-mode operation of each element can be achieved. In combination with their excellent beam quality and their independence of a third terminal and AR coatings, DBR/TO QCLs are highly suited as elements for single-mode multi-wavelength arrays as convenient sources for spectroscopy and detection systems of moderate power requirements. This conclusion is supported by the recently reported stand-off system demonstration reviewed in the following section.

9. Spectroscopy demonstrations by QCL array systems

9.1. Spectroscopy on liquids employing a DFB QCL array

A first demonstration of broadband spectroscopy employing a purely electrically tuned QCL array was presented in reference [69], using the overcoupled QCL array (3.5 mm length) discussed in Section 4, for which the spectra are shown in Fig. 1a. In order to illustrate the potential of QCL array sources in the mid-infrared, spectroscopy on liquids was demonstrated, which requires a wide spectral coverage of the spectroscopy system due to the broadening of fingerprint features as compared to gas absorption lines. The spectroscopy demonstration was performed in the setup configuration illustrated in the inset of Fig. 10a, where the test liquids are contained in a fluid cell with an optical path length of 23.6 μm, and are characterized in transmission by sequentially firing the QCL array elements while recording the transmitted power by a HgCdTe detector. In Fig. 10a, the obtained spectra of isopropanol, methanol and acetone are shown as squares, triangles and circles, respectively. The solid lines represent the respective transmission spectra as recorded with a FTIR, showing good agreement between the two spectroscopic methods. The acquisition time for the spectra recorded by switching between the array elements was less than 10 s. However, it has to be noted that this first spectroscopy demonstration was far from optimized in terms of sampling rate, and an increase in both the data transfer rate and QCL repetition frequency is predicted to reduce the acquisition time for spectra to the millisecond regime.

While the number of spectral data points are limited to the number of array elements in the case of purely switching-based tuning (Fig. 10a), the demonstrated continuous tunability of QCL arrays in principle allows achieving resolutions down to the QCL linewidth, only further limited by the acquisition time and by the accuracy of QCL temperature control. The isopropanol spectrum presented in Fig. 10b demonstrates an increase of the number of spectral points over the number of array elements by a factor of four, achieved by acquiring sequential-firing spectra at

© 2015 by WILEY-VCH Verlag GmbH & Co. KGaA, Weinheim

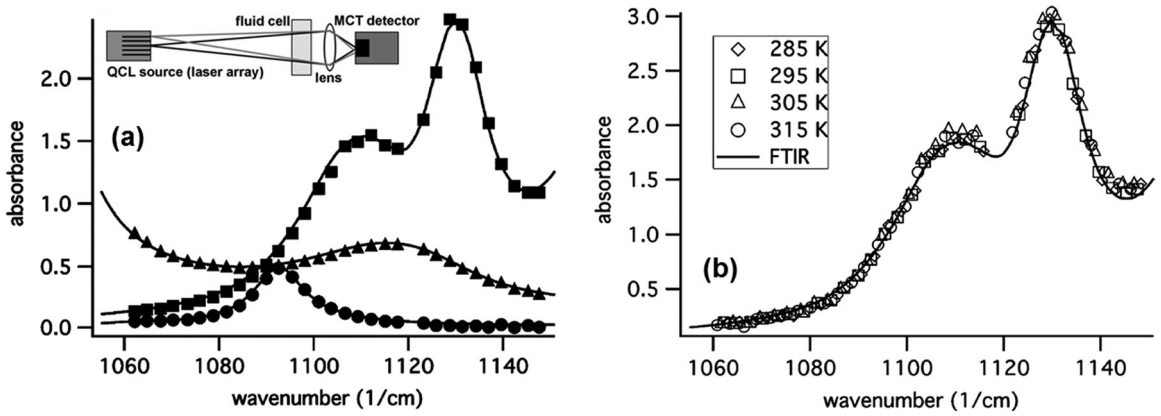

Figure 10 Spectroscopy demonstrations by DFB QCL systems. (a) Absorbance spectra acquired via transmission spectroscopy of methanol (triangles), acetone (circles) and isopropanol (squares) employing a DFB QCL array source. Purely electronic tuning of the array was performed by switching between the individual QCL elements. A fluid cell containing the liquid specimen was placed in the beam path, as illustrated in the setup schematics shown in the inset. For comparison, the solid lines show the respective absorbance spectra as measured with an FTIR. (b) Temperature tuning of the individual array elements allows a continuous spectral coverage by the QCL array, as demonstrated by the shown absorbance spectrum of isopropanol. Reproduced with permission [69]. Copyright 2009, IEEE.

different QCL temperatures. While the temperature tuning in reference [69] was performed via varying the heat-sink temperature by a thermoelectric cooler, a direct control of the QCL temperature by application of a dc current is feasible in pulsed operation, allowing wavelength sweeps over 5 cm^{-1} on the time scale of milliseconds (see Section 9.2.).

The implementation of wavelength beam combining schemes as reviewed in Section 6 allows an increase in the optical path length of a spectroscopic setup based on a QCL array, ultimately enabling the realization of stand-off detection systems. As demonstrated in reference [80], utilizing a single-grating beam-combining scheme makes an increase in the distance between the QCL array and the detector to 6 m feasible, while still maintaining the capability of performing spectroscopy. In reference [82], an extension of the free-space optical path between the array and the detector in a spectroscopy setup up to a length of 70 m was achieved by expanding the beam-combining setup into a dual-grating configuration. As a remote spectroscopy demonstration, the transmission spectrum of a polymer sample was recorded in this configuration, clearly showing the potential of beam-combined QCL arrays for stand-off detection systems.

9.2. Hyperspectral imaging employing a DBR/TO QCL array

Recently, a first hyperspectral imaging demonstration by a QCL array system has been reported based on an array of DBR/TO devices equivalent to those reviewed in Section 8 [100]. The array comprised 14 lasers operating at different wavelengths between 9.2 and 9.8 μm, where the emission was collimated by a cylindrical microlens. Wavelength beam combining of the array output in a single-grating setup (see Section 6) reduced the peak-to-peak pointing error between the devices to 0.53, supporting stand-off distances of up to 6.8 m for a beam diameter of 19 mm. In order to increase the number of wavelengths accessible by the array, the individual laser elements were tuned via changing the temperature and therefore the refractive index of the DBR sections. The DBR temperature was controlled by a long current pulse with a density below the threshold for lasing on the band-edge modes of the DBR section. Figure 11a shows that continuous thermal tuning of the array elements over 2.8 cm^{-1} can be achieved by heating with 4-μs long current pulses. In a stand-off detection setup comprising the beam-combined DBR/TO QCL source and a digital-pixel focal plane array of HgCdTe detectors, hyperspectral image cubes of a gold surface covered with diethyl phthalate (DEP) were recorded. Figure 11b shows reflectance images obtained at a stand-off distance of 5 m for illumination at two different wavenumbers (by two different array elements), one on and one off resonance with an absorption peak of the DEP. While the gold surface is clearly visible as a bright area at an illumination wavenumber of 1049 cm^{-1}, a dark blue spot appears at 1072 cm^{-1} coincidental with the DEP-covered area. The reported data therefore clearly demonstrate the successful imaging of DEP on diffusely reflecting gold at a stand-off distance of 5 m. In Fig. 11c, a reflectance spectrum of DEP recorded in the same setup is presented, demonstrating the increase of the number of spectral data points over the number of array elements by thermal tuning of the devices. Supported by the onchip data-processing architecture of the employed focal plane array, the stand-off detection system demonstrated in reference [100] was capable of high-speed differential imaging. This allowed the recording of images showing the difference in reflectance between two different illumination wavelengths at 4.1 μs per frame, where an example is presented in Fig. 11d. The image shows the difference

© 2015 by WILEY-VCH Verlag GmbH & Co. KGaA, Weinheim

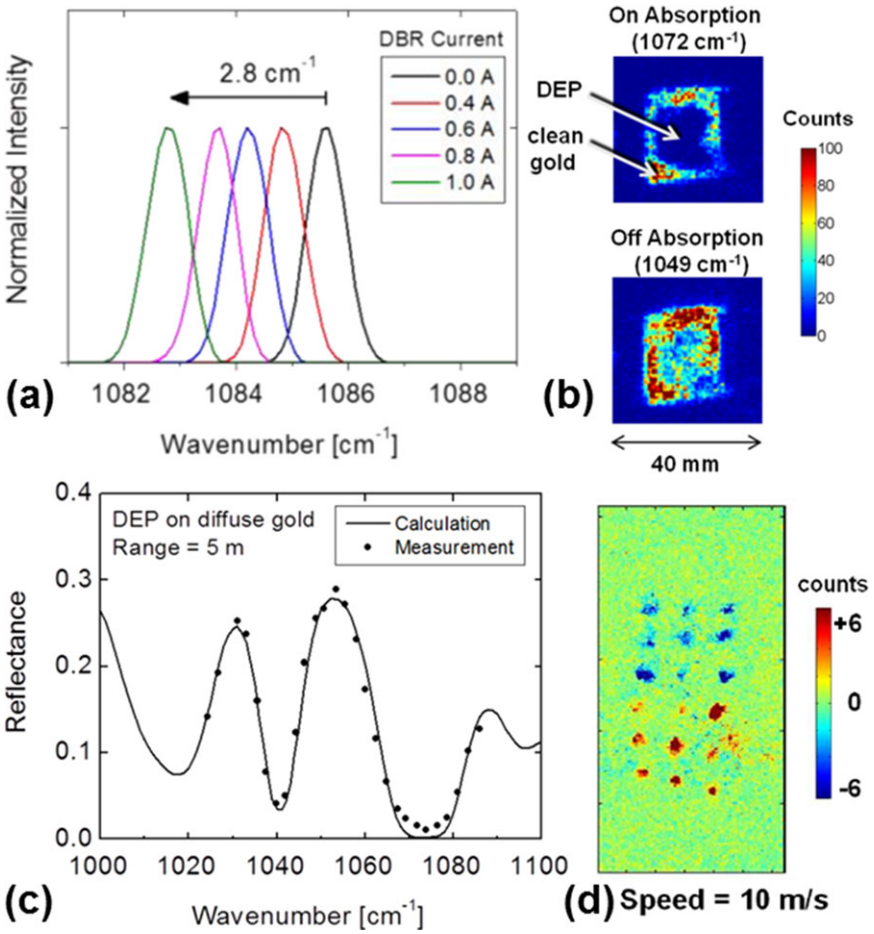

Figure 11 Hyperspectral imaging and stand-off spectroscopy demonstration by a DBR/TO QCL array system. (a) Temperature tuning of the emission wavenumber of individual array elements is achieved by current-induced heating of the DBR section. (b) Reflectance images of a gold surface covered with DEP recorded for two different illumination wavenumbers (firing of two different array elements). At a wavenumber of 1072 cm^{-1} in resonance with DEP absorption, the DEP covered area is clearly visible as a dark blue spot. (c) Reflectance spectrum of DEP on a gold surface recorded at a stand-off distance of 5 m in excellent agreement with the calculated characteristics. (d) Differential reflectance images of a target moving at 10 m/s, showing the spatially resolved difference in reflectance between two characteristic wavenumbers. The red spots indicate areas containing $KClO_3$, whereas the blue spots coincide with sand-covered regions. A short image acquisition time of 4.1 μs allows the sharp spatial resolution of the moving target. Reproduced with permission [100]. Copyright 2014, Optical Society of America.

in reflectance between the two wavelengths of 9.8 and 9.3 μm of a target moving at a speed of 10 m/s, recorded at a distance of 10 cm. The red and blue spots in the image correspond to areas on the sample covered with potassium chlorate ($KClO_3$) and sand particles, respectively, which are both clearly spatially resolved and spectrally distinguished even at these high speeds.

The results reported in reference [100] therefore demonstrate that by combining a multi-wavelength QCL array of moderate output power (only 300 mW of peak power were used) with a focal plane array allowing onchip spectral classification, spectral image acquisition times in the microsecond regime can be achieved. This tremendous potential of hyperspectral imaging systems based on QCL arrays regarding high data acquisition rates cannot be matched by EC QCL or FTIR-based systems, which can approach submillisecond data acquisition times only in very optimistic scenarios. The crucial advantage of QCL arrays is their rapid access to individual wavelengths, where switching times in the 100-kHz regime can be achieved, independent of the wavelength spacing between the individual spectral points of interest. The latter is in strong contrast to EC QCLs, where the stepping time between two wavelengths increases with their spectral spacing and stepping over 100 cm^{-1} requires up to 2 ms in state-of-the-art commercial systems. FTIR-based systems are in turn limited by the collection of large amount of data and long mirror scanning ranges required for achieving high resolutions, where independent probing of spectral points of interest is not possible due to the interferometer principle.

Therefore, in addition to being a compact, robust, maintenance-free, electrically tunable platform, QCL array systems have the potential to vastly outperform both EC QCLs and FTIRs in spectroscopy as well as stand-off and hyperspectral imaging systems, the former in acquisition speed and the latter in both speed and spectral resolution.

10. Conclusions

In the past few years, our group has reported on a series of multi-wavelength QCL arrays, each based on a different concept for the array elements. The first of these arrays were based on DFB QCLs, and single-mode emission at 32 different wavenumbers by compact chips of an equal number of elements was achieved by realizing overcoupled DFB gratings with a periodicity varying across the array. Successful wavelength beam combining as well as spectroscopy on liquids was demonstrated, where continuous tunability free of

© 2015 by WILEY-VCH Verlag GmbH & Co. KGaA, Weinheim

mechanical components was achieved by microcontrolled switching between the array elements and temperature tuning of their emission. While arrays comprising conventional single-mode DFB devices demonstrated the high suitability of QCL arrays as tunable sources for spectroscopy applications in the mid-infrared, their peak output power was rather limited and inhomogeneous across the array due to a large variation in the slope efficiencies.

By implementing the MOPA concept as a more powerful alternative to DFB devices, the peak output powers achieved by QCL arrays were tremendously increased while preserving the spectral purity and high beam quality of narrow DFB ridges. The devices of the demonstrated sixteen-element MOPA QCL array feature peak powers between 2.7 W and 10 W for single-mode emission (SMSR $\geq$ 20 dB), an order of magnitude higher than the power range accessible by the DFB QCL arrays, and superior far-field properties with narrow single-lobed intensity distributions in the chip plane exhibiting FWHM angles around 7.7°. In addition to the increase in array output power, MOPA QCL arrays exhibit far more homogeneous slope efficiencies across the chip due to the homogenizing effect of gain saturation in the amplifier section. The residual output power variation across the MOPA QCL array is not dominated by the differing slope efficiencies of the array elements, but by the onset of multi-mode operation at high MO or PA currents for several devices. The latter can be attributed to the influence of the device facets, and a suppression of the facet-mirror influence on the MOPA operation can be targeted in future arrays by either applying an AR coating to the back facet or by increasing the coupling strength of the DFB grating. Maximum peak output powers of several tens of Watts can be expected for future MOPA QCL arrays of optimized geometry, in particular with higher PA taper angles. The high output powers achieved by MOPA QCLs come at the price of a more complex device layout requiring the application of an AR coating and three terminals for driving. While this is a minor issue for most applications, the increased effort in fabrication and driving is unnecessary for spectroscopy systems with more moderate power requirements. For the latter, QCL arrays based on the DBR/TO geometry show large potential, where single-mode operation at peak output powers between 0.4 and 1.6 W have been demonstrated for a series of two-terminal devices on a chip. By further optimizing the DBR section design and geometry of these devices, proper array operation with multi-Watt single-mode emission at a series of different wavelengths can be targeted for future DBR/TO QCL chips.

In addition to their excellent figures of merit, QCL arrays are monolithic chips of small size, can be tuned by purely electronic means free of mechanical components and are highly customizable due to a large design freedom in both bandstructure and photonic engineering. The covered wavelength range and accessible peak power can be tailored by broadband material design and device geometry, respectively. The spectral resolution required by the application can be addressed by an appropriate choice of the number of array elements in combination with temperature tuning over a small wavelength range, where in principle hundreds of devices on a chip are feasible. In the case of applications requiring probing of only a few selected fingerprint wavelengths, accurately designed DFB sections can specifically target these spectral hotspots, reducing the number of array elements and increasing the detection speed. Custom-driven solutions can address high-frequency sequential firing of the array elements, allowing for short spectrum acquisition times in the microsecond regime. Furthermore, monolithic integration with additional optical components like collimators and beam combiners can be envisioned for future devices. Spectroscopy and detection systems based on multi-wavelength QCL arrays as tunable mid-infrared sources therefore have tremendous potential to outperform conventional systems like EC QCL-based platforms or FTIRs in a variety of fields and to open up new applications calling for fast, compact and mechanically robust solutions with high customizability.

Acknowledgements. We gratefully acknowledge the following people who contributed to the work presented in this paper: S. Menzel, B. G. Lee, M. A. Belkin, A. K. Goyal, C.A. Wang, A. Sanchez, G. Turner, T. Myers, M. Kelly, B. Tyrrell, R. Audet, J. MacArthur, L. Diehl, C. Pflügl, D. C. Oakley, D. Chapman, A. Napoleone, D. Bour, S. Corzine, G. Höfler, H. A. Zhang, M. Fischer, A. Wittmann, J. Kansky, O. Shatrovoy, M. Spencer and J. Faist. The authors acknowledge the Center for Nanoscale Systems (CNS) at Harvard University. Harvard CNS is a member of the National Nanotechnology Infrastructure Network (NNIN). This project received support from the Defense Threat Reduction Agency-Joint Science and Technology Office for Chemical and Biological Defense (Grant no. HDTRA1-10-1-0031-DOD). P. Rauter acknowledges support from the Austrian Science Fund (FWF): J 3092-N19.

Received: 15 April 2015, **Revised:** 25 June 2015,
Accepted: 15 July 2015

Published online: 21 August 2015

Key words: mid-infrared quantum cascade lasers, laser arrays, spectroscopy systems, master-oscillator power-amplifiers, tapered cavities.

Patrick Rauter received his M.S. degree in physics in 2003 and his Ph.D. in technical sciences in 2010, both from the Johannes Kepler University Linz. His thesis on intersubband relaxation times and optoelectronic devices in the SiGe system was supervised by Prof. Günther Bauer and Prof. Thomas Fromherz. He was awarded an Erwin Schrödinger Fellowship in 2010 granting Marie Curie Fellow status, and joined the group of Prof. Federico Capasso at Harvard University in 2011. His efforts in the Capasso group included work on high-power quantum cascade laser arrays and monolithic control of circularly polarized emission by aperture antennas. Since 2013, he is a research associate at the Institute of Semiconductor and Solid State Physics of the Johannes Kepler University Linz, where he works on the realization of a SiGe quantum cascade laser.

© 2015 by WILEY-VCH Verlag GmbH & Co. KGaA, Weinheim

Federico Capasso is the Robert L. Wallace Professor of Applied Physics and Vinton Hayes Senior Research Fellow in Electrical Engineering at Harvard University. He received a Doctor of Physics degree (summa cum laude), from the University of Rome, Italy, in 1973. After doing research in fiber optics at Fondazione Bordoni in Rome, he joined Bell Laboratory in 1976. In 1984, he was made a Distinguished Member of Technical Staff and in 1997 a Bell Labs Fellow. At Bell Labs, he held the posts of Head of the Quantum Phenomena and Device Research Department and the Semiconductor Physics Research Department between 1987 and 2000. From 2000 to 2002 he was Vice President of Physical Research at Lucent Technology. In 2003, Capasso left Bell to take up a faculty position at Harvard University. In collaboration with a wide range of multidisciplinary scientists and engineers, he has made a series of very important contributions to solid-state physics, devices, materials, and applications, including the development of low-noise quantum-well avalanche photodiodes, resonant tunneling transistors, new memory devices and the quantum cascade laser (QCL). Capasso's current research is focused on engineered surfaces that can be used to make flat optical components by phase control on a surface. Prof. Capasso is a Fellow of the American Academy of Arts and Sciences, the Institute of Physics (UK), the American Association for the Advancement of Science, the International Society for Optical Engineering (SPIE), the Optical Society of America, the IEEE and the American Physical Society. He holds four honorary doctorates, and has received numerous awards including the 2011 Galileo Galilei Medal of the Italian Society for Optics and Photonics, the 2011 Jan Czochralski Award of the European Materials Research Society, the 2010 Julius Springer Prize in Applied Physics, the 2010 Berthold Leibinger Zukunfts Preis (Future prize), and many others.

References

[1] J. Faist, F. Capasso, D. L. Sivco, C. Sirtori, A. L. Hutchinson, and A. Y. Cho, Science **22**, 553–556 (1994).
[2] C. Gmachl, F. Capasso, D. L. Sivco, and A. Y. Cho, Rep. Prog. Phys. **64** (11), 15331601 (2001).
[3] J. P. Commin, D. G. Revin, S. Y. Zhang, A. B. Krysa, K. Kennedy, and J. W. Cockburn, Appl. Phys. Lett. **97**, 031108 (2010).
[4] O. Cathabard, R. Teissier, J. Devenson, J. C. Moreno, and A. N. Baranov, Appl. Phys. Lett. **96**, 141110 (2010).
[5] A. Bismuto, M. Beck, and J. Faist, Appl. Phys. Lett. **98**, 191104 (2011).
[6] K. Vijayraghavan, Y. Jiang, M. Jang, A. Jiang, K. Choutagunta, A. Vizbaras, F. Demmerle, G. Boehm, M. C. Amann, and M. A. Belkin, Nature Commun. **4**, 2021 (2013).
[7] N. Yu, J. Fan, Q. Wang, C. Pfügl, L. Diehl, T. Edamura, M. Yamanishi, H. Kan, and F. Capasso, Nature Photon. **2**, 564 (2008).
[8] F. Capasso, Opt. Eng. **49**, 111102 (2010).
[9] Y. Yao, A. J. Hoffman, and C. F. Gmachl, Nature Photon. **6**, 432 (2012).
[10] G. Scalari, C. Walther, M. Fischer, R. Terazzi, H. Beere, D. Ritchie, and J. Faist, Laser Photon. Rev. **3** (1–2), 45–66 (2009).
[11] S. Kumar, IEEE J. Sel. Top. Quant. Electron. **17** (1), 38–47 (2011).
[12] D. Heydari, Y. Bai, N. Bandyopadhyay, S. Slivken, and M. Razeghi, Appl. Phys. Lett. **106**, 091105 (2015).
[13] Y. Bai, S. Slivken, Q. Y. Lu, N. Bandyopadhyay, and M. Razeghi, Appl. Phys. Lett. **101**, 081106 (2012).
[14] B. Gokden, Y. Bai, N. Bandyopadhyay, S. Slivken, and M. Razeghi, Appl. Phys. Lett. **97**, 131112 (2010).
[15] Q. Y. Lu, Y. Bai, N. Bandyopadhyay, S. Slivken, and M. Razeghi, Appl. Phys. Lett. **98**, 181106 (2011).
[16] L. Li, L. Chen, J. Zhu, J. Freeman, P. Dean, A. Valavanis, A. G. Davies, and E. H. Linfield, Electron. Lett. **4**, 309 (2014).
[17] M. Brandstetter, C. Deutsch, M. Krall, H. Detz, D. C. MacFarland, T. Zederbauer, A. M. Andrews, W. Schrenk, G. Strasser, and K. Unterrainer, Appl. Phys. Lett. **103**, 171113 (2013).
[18] R. F. Curl, F. Capasso, C. Gmachl, A. A. Kosterev, B. McManuse, R. Lewicki, M. Pusharsky, G. Wysockic, and F. K. Tittel, Chem. Phys. Lett. **487**, 1–18 (2010).
[19] C. Wang and P. Sahay, Sensors **2009**, 8230 (2009).
[20] J. Mandon, M. Högman, P. J. F. M. Merkus, J. van Amsterdam, F. J. M. Harren, and S. M. Cristescu, J. Biomed. Opt. **17**, 017003 (2012).
[21] Y.-C. Chang, P. Wägli, V. Paeder, A. Homsy, L. Hvozdara, P. van der Wal, J. Di Francesco, N. F. de Rooij, and H. P. Herzig, Lab Chip **12**, 3020 (2012).
[22] B. Schwarz, P. Reininger, D. Ristanic, H. Detz, A. M. Andrews, W. Schrenk, and G. Strasser, Nature Commun. **5**, 4085 (2014).
[23] R. Lewicki, J. H. Doty III, R. F. Curl, F. K. Tittel, and G. Wysocki, Proc. Natl. Acad. Sci. USA **106**, 12587 (2009).
[24] M. Pushkarsky, A. Tsekoun, I. G. Dunayevskiy, R. Go, and C. K. N. Patel, Proc. Natl. Acad. Sci. USA **103**, 10846 (2006).
[25] Y. Ma, R. Lewicki, M. Razeghi, and F. K. Tittel, Opt. Exp. **21**, 1008 (2013).
[26] W. Ren, W. Jiang, N. P. Sanchez, P. Patimisco, V. Spagnolo, C. Zah, F. Xie, L. C. Hughes, R. J. Griffin, and F. K. Tittel, Appl. Phys. Lett. **104**, 041117 (2014).
[27] S. Borri, P. Patimisco, I. Galli, D. Mazzotti, G. Giusfredi, N. Akikusa, M. Yamanishi, G. Scamarcio, P. De Natale, and V. Spagnolo, Appl. Phys. Lett. **104**, 091114 (2014).
[28] H. Yi, R. Maamary, X. Gao, M. W. Sigrist, E. Fertein, and W. Chen, Appl. Phys. Lett. **106**, 101109 (2015).
[29] M. B. Pushkarsky, I. G. Dunayevskiy, M. Prasanna, A. G. Tsekoun, R. Go, and C. K. N. Patel, Proc. Natl. Acad. Sci. USA **103**, 19630 (2006).
[30] F. Fuchs, S. Hugger, M. Kinzer, R. Aidam, W. Bronner, and R. Lösch, Opt. Eng. **49**, 111127 (2010)
[31] C. A. Kendziora, R. M. Jones, R. Furstenberg, M. Papantonakis, V. Nguyen, and R. A. McGill, Proc. SPIE **8373**, 83732H (2012).
[32] S. Hugger, F. Fuchs, J. Jarvis, M. Kinzer, Q. K. Yang, R. Driad, R. Aidam, and J. Wagner, Proc. SPIE **8631**, 86312I–1 (2013).
[33] K. Yeh, S. Kenkel, J.-N. Liu, and R. Bhargava, Anal. Chem. **87**, 485–493 (2014).

© 2015 by WILEY-VCH Verlag GmbH & Co. KGaA, Weinheim

[34] N. Kröger, A. Egl, M. Engel, N. Gretz, K. Haase, I. Herpich, B. Kränzlin, S. Neudecker, A. Pucci, A. Schönhals, J. Vogt, and W. Petrich, J. Biomed. Opt. **19** (11), 111607 (2014).
[35] P. Bassan, M. J. Weida, J. Rowlette, and P. Gardner, Analyst **139**, 3856–3859 (2014).
[36] J. Faist, M. Beck, T. Aellen, and E. Gini, Appl. Phys. Lett. **78**, 147 (2001).
[37] A. Wittmann, T. Gresch, E. Gini, L. Hvozdara, N. Hoyler, M. Giovannini, and J. Faist, IEEE J. Quantum Electron. **44**, 36 (2008).
[38] C. Gmachl, D. L. Sivco, R. Colombelli, F. Capasso, and A. Y. Cho, Nature **415**, 883 (2002).
[39] R. Maulini, A. Mohan, M. Giovannini, J. Faist, and E. Gini, Appl. Phys. Lett. **88**, 201113 (2006).
[40] K. Fujita, T. Edamura, S. Furuta, and M. Yamanishi, Appl. Phys. Lett. **96**, 241107 (2010).
[41] Y. Yao, X. Wang, J.-Y. Fan, and C. F. Gmachl, Appl. Phys. Lett. **97**, 081115 (2010).
[42] C. Gmachl, A. Straub, R. Colombelli, F. Capasso, D. L. Sivco, A. M. Sergent, and A. Y. Cho, IEEE J. Quantum Electron. **38**, 569 (2002).
[43] For a review on external cavity QCLs see: A. Hugi, R. Maulini, and J. Faist, Semicond. Sci. Technol. **25**, 083001 (2010).
[44] G. Luo, C. Peng, H. Q. Le, S.-S. Pei, H. Lee, W.-Y. Hwang, B. Ishaug, and J. Zheng, IEEE J. Quantum Electron. **38**, 486 (2002).
[45] A. Hugi, R. Terazzi, Y. Bonetti, A. Wittmann, M. Fischer, M. Beck, J. Faist, and E. Gini, Appl. Phys. Lett. **95**, 061103 (2009).
[46] S. Riedi, A. Hugi, A. Bismuto, M. Beck, and J. Faist, Appl. Phys. Lett. **103**, 031108 (2013).
[47] G. Wysocki, R.F. Curl, F.K. Tittel, R. Maulini, J. M. Bulliard, and J. Faist, Appl. Phys. B **81**, 769 (2005).
[48] T. S. Mansuripur, S. Menzel, R. Blanchard, L. Diehl, C. Pflügl, Y. Huang, J.-H. Ryou, R. D. Dupuis, M. Loncar, and F. Capasso, Opt. Exp. **20**, 23339 (2012).
[49] S. Slivken, N. Bandyopadhyay, Y. Bai, Q. Y. Lu, and M. Razeghi, Appl. Phys. Lett. **103**, 231110 (2013).
[50] S. Kalchmair, R. Blanchard, T. S. Mansuripur, G.-M. de Naurois, C. Pflügl, M. F. Witinski, L. Diehl, F. Capasso, and M. Loncar, Opt. Exp. **23**, 15734 (2015).
[51] A. Foltynowicz, T. Ban, P. Masłowski, F. Adler, and J. Ye, Phys. Rev. Lett. **107**, 233002 (2011).
[52] I. Coddington, W. C. Swann, and N. R. Newbury, Phys. Rev. Lett. **100**, 013902 (2008).
[53] F. Keilmann, C. Gohle, and R. Holzwarth, Opt. Lett. **29**, 1542 (2004).
[54] A. Hugi, G. Villares, S. Blaser, H. C. Liu, and J. Faist, Nature **492**, 229 (2012).
[55] Q. Y. Lu, M. Razeghi, S. Slivken, N. Bandyopadhyay, Y. Bai, W. J. Zhou, M. Chen, D. Heydari, A. Haddadi, R. McClintock, M. Amanti, and C. Sirtori, Appl. Phys. Lett. **106**, 051105 (2015).
[56] D. Burghoff, T.-Y. Kao, N. Han, C. W. I. Chan, X. Cai, Y. Yang, D. J. Hayton, J.-R. Gao, J. L. Reno, and Q. Hu, Nature Photon. **8**, 462–467 (2014).
[57] A. K. Wojcik, P. Malara, R. Blanchard, T. S. Mansuripur, F. Capasso, and A. Belyanin, Appl. Phys. Lett. **103**, 231102 (2013).
[58] P. Malara, R. Blanchard, T. S. Mansuripur, A. K. Wojcik, A. Belyanin, K. Fujita, T. Edamura, S. Furuta, M. Yamanishi, P. de Natale, and F. Capasso, Appl. Phys. Lett. **102**, 141105 (2013).
[59] Y. Wang, M. G. Soskind, W. Wang, and G. Wysocki, Appl. Phys. Lett. **104**, 031114 (2014).
[60] G. Villares, A. Hugi, S. Blaser, and J. Faist, Nature Commun. **5**, 5192 (2014).
[61] J. D. Kirch, C.-C. Chang, C. Boyle, L. J. Mawst, D. Lindberg III, T. Earles, and D. Botez, Appl. Phys. Lett. **106**, 061113 (2015).
[62] L. K. Hoffmann, M. Klinkmüller, E. Mujagic, M. P. Semtsiv, W. Schrenk, W. T. Masselink, and G. Strasser, Opt. Exp. **17**, 649 (2009).
[63] G. M. de Naurois, M. Carras, B. Simozrag, O. Patard, F. Alexandre, and X. Marcadet, AIP Adv. **1**, 032165 (2011).
[64] T.-Y. Kao, Q. Hu, and J. L. Reno, Appl. Phys. Lett. **96**, 101106 (2010).
[65] J. Faist, C. Gmachl, F. Capasso, C. Sirtori, D. L. Sivco, J. N. Baillargeon, and A. Y. Cho, Appl. Phys. Lett. **70**, 2670 (1997).
[66] H. Kogelnik and C. V. Shank, J. Appl. Phys. **43**, 2327 (1972).
[67] B. G. Lee, M. A. Belkin, R. Audet, J. MacArthur, L. Diehl, C. Pflügl, F. Capasso, D. C. Oakley, D. Chapman, A. Napoleone, D. Bour, S. Corzine, G. Höfler, and J. Faist, Appl. Phys. Lett. **91**, 231101 (2007).
[68] R. Maulini, M. Beck, J. Faist, and E. Gini, Appl. Phys. Lett. **84**, 1659 (2004).
[69] B. G. Lee, M. A. Belkin, C. Pflügl, L. Diehl, H. A. Zhang, R. M. Audet, J. MacArthur, D. P. Bour, S. W. Corzine, G. E. Höfler, and F. Capasso, IEEE J. Quantum Electron. **45**, 554 (2009).
[70] B. G. Lee, H. A. Zhang, C. Pflügl, L. Diehl, M. A. Belkin, M. Fischer, A. Wittmann, J. Faist, and F. Capasso, IEEE Photon. Technol. Lett. **21**, 914 (2009).
[71] M. Carras, G. Maisons, B. Simozrag, V. Trinite, M. Brun, G. Grand, P. Labeye, and S. Nicoletti, Proc. SPIE **8631**, 863113 (2013).
[72] M. Carras, G. Maisons, B. Simozrag, M. Garcia, O. Parillaud, J. Massies, and X. Marcadet, Appl. Phys. Lett. **96**, 161105 (2010).
[73] W. Streifer, R. D. Durnham, and D. Scifres, IEEE J. Quantum Electron. **11**, 154 (1975).
[74] M. Sidler, P. Rauter, R. Blanchard, P. Métivier, T. S. Mansuripur, C. Wang, Y. Huang, J.-H. Ryou, R. D. Dupuis, J. Faist, and F. Capasso, Appl. Phys. Lett. **104**, 051102 (2014).
[75] E. Mujagic, C. Schwarzer, Y. Yao, J. Chen, C. Gmachl, and G. Strasser, Appl. Phys. Lett. **98**, 141101 (2011).
[76] Y. Yao, W. O. Charles, T. Tsai, J. Chen, G. Wysocki, and C. F. Gmachl, Appl. Phys. Lett. **96**, 211106 (2010).
[77] E. Mujagic, L. K. Hoffmann, S. Schartner, M. Nobile, W. Schrenk, M. P. Semtsiv, M. Wienold, W. T. Masselink, and G. Strasser, Appl. Phys. Lett. **93**, 161102 (2008).
[78] C. Schwarzer, R. Szedlak, S. Il Ahn, T. Zederbauer, H. Detz, A. M. Andrews, W. Schrenk, and G. Strasser, Appl. Phys. Lett. **103**, 081101 (2013).
[79] P. Jouy, C. Bonzon, J. Wolf, E. Gini, M. Beck, and J. Faist, Appl. Phys. Lett. **106**, 071104 (2015).

© 2015 by WILEY-VCH Verlag GmbH & Co. KGaA, Weinheim

[80] B. G. Lee, J. Kansky, A. K. Goyal, C. Pflügl, L. Diehl, M. A. Belkin, A. Sanchez, F. Capasso, Proc. SPIE **7460**, 746004 (2009).
[81] T. Y. Fan, IEEE J. Sel. Top. Quantum Electron. **11**, 567 (2005).
[82] A. K. Goyal, M. Spencer, O. Shatrovoy, B. G. Lee, L. Diehl, C. Pfluegl, A. Sanchez, and F. Capasso, Opt. Exp. **19**, 26725 (2011).
[83] D. F. Welch, D. Mehuys, R. Parke, R. Waarts, D. Scifres, and W. Streifer, Electron. Lett. **26**, 1327 (1990).
[84] D. F. Welch, R. Parke, D. Mehuys, A. Hardy, R. Lang, S. Obrien, and S. Scifres, Electron. Lett. **28**, 2011 (1992).
[85] H. Wenzel, K. Paschke, O. Brox, F. Bugge, J. Fricke, A. Ginolas, A. Knauer, P. Ressel, and G. Erbert, Electron. Lett. **43**(3), 160 (2007).
[86] M. Troccoli, C. Gmachl, F. Capasso, D. L. Sivco, and A. Y. Cho, Appl. Phys. Lett. **80**(22), 4103 (2002).
[87] S. Menzel, L. Diehl, C. Pflügl, A. Goyal, C. Wang, A. Sanchez, G. Turner, and F. Capasso, Opt. Exp. **19**, 16229 (2011).
[88] B. Hinkov, M. Beck, E. Gini, and J. Faist, Opt. Exp. **21**, 19180 (2013).
[89] J. N. Walpole, Opt. Quantum Electron. **28**, 623 (1996).
[90] P. Rauter, S. Menzel, A. K. Goyal, B. Gökden, C.A. Wang, A. Sanchez, G. Turner, and F. Capasso, Appl. Phys. Lett. **101**, 261117 (2012).
[91] P. Rauter, S. Menzel, A. K. Goyal, C.A. Wang, A. Sanchez, G. Turner, and F. Capasso, Opt. Exp. **21**, 4518 (2013).
[92] R. Blanchard, T. S. Mansuripur, B. Gökden, N. Yu, M. Kats, P. Genevet, K. Fujita, T. Edamura, M. Yamanishi, and F. Capasso, Appl. Phys. Lett. **102**, 191114 (2013).
[93] H. A. Haus and C. V. Shank, IEEE J. Quantum Electron. **12**, 532 (1976).
[94] K. Utaka, S. Akiba, K. Sakai, and Y. Matsushima, IEEE J. Quantum Electron. **22**, 1042 (1986).
[95] M. Usami, S. Akiba, and K. Utaka, IEEE J. Quantum Electron. **23**, 815 (1987).
[96] L. Nähle, J. Semmel, W. Kaiser, S. Höfling, and A. Forchel, Appl. Phys. Lett. **91**, 181122 (2007).
[97] B. Gökden, T. S. Mansuripur, R. Blanchard, C. Wang, A. Goyal, A. Sanchez-Rubio, G. Turner, and F. Capasso, Appl. Phys. Lett. **102**, 053503 (2013).
[98] B. Sumpf, K.-H. Hasler, P. Adamiec, F. Bugge, F. Dittmar, J. Fricke, H. Wenzel, M. Zorn, G. Erbert, and G. Tränkle, IEEE J. Sel. Top. Quantum Electron. **15**, 1009 (2009).
[99] P. Rauter, S. Menzel, B. Gokden, A. K. Goyal, C. A. Wang, A. Sanchez, G. Turner, and F. Capasso, Appl. Phys. Lett. **102**, 181102 (2013).
[100] A. Goyal, T. Myers, C. A. Wang, M. Kelly, B. Tyrrell, B. Gokden, A. Sanchez, G. Turner, and F. Capasso, Opt. Exp. **22** (12), 14392–14401 (2014).

© 2015 by WILEY-VCH Verlag GmbH & Co. KGaA, Weinheim